

Simultaneous evidence of edge collapse and hub-filament configurations: A rare case study of a Giant Molecular Filament G45.3+0.1

N. K. BHADARI,^{1,2} L. K. DEWANGAN,¹ D. K. OJHA,³ L. E. PIROGOV,⁴ AND A. K. MAITY^{1,2}

¹*Astronomy & Astrophysics Division, Physical Research Laboratory, Navrangpura, Ahmedabad 380009, India*

²*Indian Institute of Technology Gandhinagar Palaj, Gandhinagar 382355, India.*

³*Department of Astronomy and Astrophysics, Tata Institute of Fundamental Research, Homi Bhabha Road, Mumbai 400005, India.*

⁴*Institute of Applied Physics of the Russian Academy of Sciences, 46 Ulyanov st., Nizhny Novgorod 603950, Russia.*

ABSTRACT

We study multiwavelength and multiscale data to investigate the kinematics of molecular gas associated with the star-forming complexes G045.49+00.04 (G45E) and G045.14+00.14 (G45W) in the Aquila constellation. An analysis of the FUGIN ¹³CO(1–0) line data unveils the presence of a giant molecular filament (GMF G45.3+0.1; length ~ 75 pc, mass $\sim 1.1 \times 10^6 M_{\odot}$) having a coherent velocity structure at $[53, 63]$ km s^{−1}. The GMF G45.3+0.1 hosts G45E and G45W complexes at its opposite ends. We find large scale velocity oscillations along GMF G45.3+0.1, which also reveals the linear velocity gradients of -0.064 and $+0.032$ km s^{−1} pc^{−1} at its edges. The photometric analysis of point-like sources shows the clustering of young stellar object (YSO) candidate sources at the filament's edges where the presence of dense gas and HII regions are also spatially observed. The *Herschel* continuum maps along with the CHIMPS ¹³CO(3–2) line data unravel the presence of parsec scale hub-filament systems (HFSs) in both the sites, G45E and G45W. Our study suggests that the global collapse of GMF G45.3+0.1 is end-dominated, with addition to the signature of global nonisotropic collapse (GNIC) at the edges. Overall, GMF G45.3+0.1 is the first observational sample of filament where the edge collapse and the hub-filament configurations are simultaneously investigated. These observations open up the new possibility of massive star formation, including the formation of HFSs.

Keywords: dust, extinction – HII regions – ISM: clouds – ISM: individual object (IRAS 19120+1103, IRAS 19117+1107, IRAS 19111+1048 and IRAS 19110+1045) – stars: formation – stars: pre-main sequence

1. INTRODUCTION

Based on the analysis of infrared and submillimeter continuum maps, networks of filaments or hub-filament systems (HFSs; Myers 2009) have been recognized as potential birthplaces of massive stars and clusters of young protostars (e.g., André et al. 2010; Schneider et al. 2012; Anderson et al. 2021), and such HFSs are commonly detected structures in our Galaxy (e.g., Motte et al. 2018, see references therein). In general, the HFS is a junction of multiple filaments. In such configurations, filaments can be depicted with high aspect ratio (length/diameter), and the central hub is identified with low aspect ratio (e.g., Myers

2009). Molecular line observations unveil that the filaments in HFSs act as a channel of material flows to feed the dense clumps/cores (e.g., Kirk et al. 2013; Peretto et al. 2013; Dewangan et al. 2017b; Hacar et al. 2018; Treviño-Morales et al. 2019; Chen et al. 2020b; Dewangan et al. 2020; Dewangan 2021; Dewangan et al. 2022), where massive stars and young stellar clusters are observed (Liu et al. 2012; Treviño-Morales et al. 2019, and references therein). In addition to the HFSs, isolated filaments associated with star-forming activities have also been identified in our Galaxy. In particular, concerning isolated filaments, the onset of the end-dominated collapse (EDC; or edge collapse) process has been reported in a very few star-forming sites (including HII regions powered by massive stars; Dewangan et al. 2017a, 2019; Bhadari et al. 2020, and references therein), where one exclusively expects two clumps/cores produced at the respective end of filament

via high gas acceleration (e.g., Bastien 1983; Pon et al. 2012; Clarke & Whitworth 2015; Hoemann et al. 2022). These observed configurations directly manifest the role of filaments in star formation processes. However, no attempt has been made to explore the connection between these two distinct filament configurations. In this context, the present paper deals with two major star-forming complexes (i.e., G045.49+00.04 and G045.14+00.14) located in the Aquila constellation ($l=45^\circ$, $b=0^\circ$). These sites were primarily identified and catalogued as extended clouds with the prefix name of Galactic Ring Survey Molecular Cloud (GRSMC; see more details in Rathborne et al. 2009).

The two complexes are well known for hosting massive star-forming regions, numerous ultracompact (UC) HII regions, maser emission, and outflow activities from young stars including massive star(s) (e.g., Wood & Churchwell 1989; Blum & McGregor 2008; Paron et al. 2009; Rivera-Ingraham et al. 2010). The eastern complex G045.49+00.04 (hereafter, G45E) harbors the sources IRAS 19120+1103 (or G45.45+0.06) and IRAS 19117+1107 (or G45.48+0.13), while the western complex G045.14+00.14 (hereafter, G45W) hosts two active massive star-forming regions (IRAS 19110+1045 and IRAS 19111+1048). Both the complexes have been well explored using the infrared, submillimeter, and radio data sets (e.g., Vig et al. 2006; Rivera-Ingraham et al. 2010). In particular, the eastern complex is associated with the significant extended submillimeter emission (see Figure 2 in Rivera-Ingraham et al. 2010). In the direction of the western complex, the distribution of dust and ionized gas around IRAS 19110+1045 is less extended than that of IRAS 19111+1048 (Vig et al. 2006), and the former source is observed to be much younger than the other one (Hunter et al. 1997; Vig et al. 2006). A mid-infrared (MIR) view of an area containing G45E and G45W is presented in Figure 1, which is a 3-color composite map made using the *Spitzer* 24 μm (red), *WISE* 12 μm (green), and *Spitzer* 8 μm (blue) images.

Figure 1 is also overlaid with the positions of the APEX Telescope Large Area Survey of the Galaxy (ATLASGAL; Schuller et al. 2009) dust continuum clumps at 870 μm identified by Urquhart et al. (2018). Radial velocity and distance information of each ATLASGAL clump are available (see Urquhart et al. 2018, for more details). In Figure 1, the ATLASGAL 870 μm dust clumps are marked by red diamonds and blue diamonds, and are traced in a velocity range of $[55.5, 62.2]$ km s^{-1} . The clumps shown with red diamonds and blue diamonds are located at the kinematic distances of 8.4 kpc and 8 kpc, respectively. However, based on the spatial

distribution of the ATLASGAL clumps, and the morphology of the parent molecular cloud toward the sites G45E and G45W (Section 3.1), we adopt a distance of 8 kpc for both the sites in this paper. Previously, distances to these sites were considered in the range of ~ 6 –8 kpc (see Rivera-Ingraham et al. 2010, and references therein). A careful study of the molecular gas containing both the complexes is yet to be carried out. Such study is essential to probe the ongoing physical processes and will also allow us to explore the HFSs and EDC scenarios. In this relation, the submillimeter continuum maps are also utilized to carefully examine the observed spatial structures.

We organize this paper into five major sections. Section 2 describes data sets used in this paper. In Section 3, we present the results obtained using the continuum and line data. In Section 4, we discuss the implications of our derived results for explaining the star formation processes. A summary of this work is given in Section 5.

2. DATA SETS

In this work, we analyzed the publically available multiscale and multiwavelength data sets toward our target region, primarily in the area of $0^\circ.67 \times 0^\circ.50$ or 93.5×70.4 pc^2 (centred at $l = 45^\circ.30$; $b = 0^\circ.05$). The overview of data sets used in this work is presented in Table 1. We utilized the $^{12}\text{CO}(J=1-0)$, $^{13}\text{CO}(J=1-0)$, and $\text{C}^{18}\text{O}(J=1-0)$ line data obtained from the FOREST Unbiased Galactic plane Imaging survey with the Nobeyama 45-m telescope (FUGIN) survey. The FUGIN data are calibrated in main beam temperature (T_{mb}), and the typical rms is ~ 1.5 K for ^{12}CO and ~ 0.7 K for ^{13}CO and C^{18}O lines. The survey data provide a velocity resolution of 1.3 km s^{-1} (see more details in Umemoto et al. 2017). We also used $^{13}\text{CO}(J=3-2)$, and $\text{C}^{18}\text{O}(J=3-2)$ line data downloaded from the $^{13}\text{CO}/\text{C}^{18}\text{O}$ ($J = 3 \rightarrow 2$) Heterodyne Inner Milky Way Plane Survey (CHIMPS). The high-resolution ($\theta_{\text{spatial}}=15''$, $\theta_{\text{velocity}}=0.5$ km s^{-1}) CHIMPS survey covers the Galactic plane within $|b| \leq 0^\circ.5$ and $28^\circ \lesssim l \lesssim 46^\circ$. The survey data have a median rms of ~ 0.6 K, and are calibrated in antenna temperature (T_{A}^*) scale. We converted the intensity scales from T_{A}^* to T_{mb} by using the relation $T_{\text{mb}} = \frac{T_{\text{A}}^*}{\eta_{\text{mb}}}$, where the mean detector efficiency is $\eta_{\text{mb}} = 0.72$ (Rigby et al. 2016). In order to improve the sensitivity, the molecular line data from the FUGIN and CHIMPS were smoothed with a Gaussian function having 3 pixels half-power beamwidth. This exercise yields the final spatial resolutions of the FUGIN and CHIMPS molecular line data to be $21''.73$ and $16''.82$, respectively.

Table 1. List of multiwavelength surveys used in this paper

Survey	Wavelength/line(s)	Angular Resolution (″)	Reference
Multi-Array Galactic Plane Imaging Survey (MAGPIS)	20 cm	~6	Helfand et al. (2006)
FUGIN	^{12}CO , ^{13}CO , C^{18}O (J=1–0)	~20	Umamoto et al. (2017)
CHIMPS	^{13}CO , C^{18}O (J=3–2)	~15	Rigby et al. (2016)
APEX Telescope Large Area Survey of the Galaxy (ATLASGAL)	870 μm	~19.2	Schuller et al. (2009)
<i>Herschel</i> Infrared Galactic Plane Survey (Hi-GAL)	70, 160, 250, 350, 500 μm	~6, 12, 18, 25, 37	Molinari et al. (2010)
Spitzer MIPS Inner Galactic Plane Survey (MIPSGAL)	24 μm	~6	Carey et al. (2005)
Wide Field Infrared Survey Explorer (WISE)	12 μm	~6.5	Wright et al. (2010)
<i>Spitzer</i> Galactic Legacy Infrared Mid-Plane Survey Extraordinaire (GLIMPSE)	3.6, 4.5, 5.8, 8.0 μm	~2	Benjamin et al. (2003)
UKIRT near-infrared Galactic Plane Survey (GPS)	1.25–2.2 μm	~0.8	Lawrence et al. (2007)
Two Micron All Sky Survey (2MASS)	1.25–2.2 μm	~2.5	Skrutskie et al. (2006)

3. RESULTS

3.1. Kinematics of molecular gas

In this section, we study the spatial-kinematic structures of the molecular gas in the direction of our target sites.

3.1.1. Morphology of the molecular cloud

In Figure 2a, we display a three-color composite map (Red: ATLASGAL 870 μm , Green: *Herschel* 350 μm , Blue: *Herschel* 160 μm) at submillimeter wavelengths of the target area presented in Figure 1. The map unravels the presence of elongated structures (or filaments) in both the star-forming complexes, G45E and G45W. Figures 2b and 2c show the ATLASGAL 870 μm continuum images overlaid with the MAGPIS 20 cm radio contours for the sites G45E and G45W, respectively. The MAGPIS radio contours display the zones of ionized emission or the HII regions in the target sites.

In order to study the kinematics of the parent molecular cloud, we have extracted the averaged molecular spectra toward a rectangular strip that passes through both the major star-forming complexes (see dotted dashed rectangle in Figure 2a). Figure 3a presents the averaged spectra of different molecular species (i.e., FUGIN $^{12}\text{CO}/^{13}\text{CO}/\text{C}^{18}\text{O}$ (1–0), CHIMPS $^{13}\text{CO}/\text{C}^{18}\text{O}$ (3–2)). The various line profiles suggest that the molecular cloud can be studied in a velocity range of [50, 70] km s^{-1} . The ^{12}CO (1–0) profile appears much broader than the other line profiles, which can be explained due to the high optical depth and lower critical density of ^{12}CO (1–0). In general, the ^{12}CO (1–0) line data are known to only trace the outer diffuse cloud. Hence, we considered a relatively optically thin ^{13}CO (1–0) line data to depict the molecular cloud boundary. The curve_fit function from the SciPy library (Virtanen et al. 2020) is employed to fit the ^{13}CO (1–0) spectra with double Gaussian profiles. The fitted Gaussian profiles along with the original ^{13}CO (1–0) profile are shown in Figure 3b. The major Gaussian component is traced in a velocity range of [53, 63] km s^{-1} , and the fitting procedure gives the mean (μ) and standard deviation (σ) to be 58.30 ± 0.03

km s^{-1} and $2.34 \pm 0.03 \text{ km s}^{-1}$, respectively. The other Gaussian component is associated with $\mu = 65.01 \pm 0.20 \text{ km s}^{-1}$ and $\sigma = 2.43 \pm 0.19 \text{ km s}^{-1}$, and contributes to the redder tail of the observed ^{13}CO (1–0) profile.

In Figure 4, we have shown the spatial distribution of the molecular cloud at [53, 63] km s^{-1} associated with the major Gaussian component. Figure 4a displays the integrated intensity (moment-0) map of ^{13}CO (1–0) emission, which is also overlaid with the C^{18}O (1–0) emission contours. The ^{13}CO (1–0) moment-0 map reveals the presence of an elongated molecular cloud that hosts the two previously star-forming complexes, G45E and G45W, at its ends. The C^{18}O (1–0) emission further unveils the dense substructures in the direction of major massive star-forming sites (i.e., IRAS 19120+1103, IRAS 19117+1107, IRAS 19110+1045 and IRAS 19111+1048).

The intensity weighted mean velocity (moment-1) map of the ^{13}CO (1–0) emission is shown in Figure 4b. A continuous velocity structure around 58 km s^{-1} further supports the idea of an elongated molecular cloud. We can also notice a relatively redshifted emission around 63 km s^{-1} , which belongs to the minor Gaussian component (Figure 3). However, the moment maps related to the minor Gaussian component are not studied in this paper. The intensity weighted linewidth map, which is generally known as the moment-2 map, is shown in Figure 4c. The linewidth value is about $\sim 2\text{--}5 \text{ km s}^{-1}$ throughout the cloud structure. There are clear velocity dispersion enhancements at the edges of the cloud, which are of the order of $\sim 4.5 \text{ km s}^{-1}$. We have also displayed the moment maps of ^{13}CO (3–2) emission in Figures 4d, 4e, and 4f. The ^{13}CO (3–2) emission traces the dense gas compared to the ^{13}CO (1–0) emission, thus allowing us to study the structures and kinematics of dense molecular clumps. From Figures 4a and 4d, the dense gas/clumps are primarily identified towards the ends of elongated cloud, and the entire cloud structure is traced in the ^{13}CO (1–0) emission only. Overall, Figure 4 collectively displays the spatial-kinematic distribution of molecular cloud associated with the target sites G45E and G45W.

To examine the velocity distribution of the gas toward the elongated cloud observed in a velocity range of [53, 63] km s⁻¹, we have shown the velocity channel maps in Figure 5. To infer the gas motion in the direction of the cloud, in Figure 5, we have also shown the C¹⁸O(3–2) integrated emission contour (in red) at a level of 3.2 K km s⁻¹. The elongated cloud morphology starts to appear from 55.67 km s⁻¹ and takes a complete shape in the velocity range from 57.62 km s⁻¹ to 59.58 km s⁻¹. The dense substructures are mostly seen at the edges of the elongated cloud.

3.1.2. Position-velocity diagrams

We have also examined the position-velocity (pv) diagrams to infer the kinematics of molecular gas. A pv diagram is an important tool to investigate the gas motion along any spatial axis. The longitude-velocity (l - v) and latitude-velocity (b - v) diagrams are displayed in Figures 6a and 6b, respectively. We have also overlaid the positions of ATLASGAL dust clumps on the l - v and b - v diagrams, showing the spatial and velocity association of the dust clumps with the cloud. A pv diagram along a selected path (physical length ~ 75 pc) is shown in Figure 6c. This path is highlighted by a dashed (red) curve in Figure 4a. Several small circular regions (radii $\sim 15''$) along this path are also selected, and an average ¹³CO(1–0) profile over each circular region is produced. For each average profile, the peak velocity is derived through the fitting of a Gaussian function. In Figure 6c, to study the pattern of velocity, we have also overlaid the peak velocity of each observed ¹³CO(1–0) profile. In the pv diagram, the velocity distribution along the path shows an oscillatory pattern, and has a maximum velocity variation of ~ 4 km s⁻¹. In addition to the oscillatory pattern, the velocity profile shows the linear gradient at both ends of the filament. In the direction of G45E, the velocity gradient is observed to have a value of -0.064 km s⁻¹ pc⁻¹, while it is $+0.032$ km s⁻¹ pc⁻¹ toward G45W. Figure 7a highlights two straight lines, indicating the presence of different velocity gradients in the pv plot (see also Figure 6c). We also note that the largest velocity gradient (~ 0.5 km s⁻¹ pc⁻¹) is associated with the western border of G45E. This signature could be an indication of accelerated gas motions. The residual velocity profile is shown in Figure 7b, which is generated after removing the mentioned velocity gradients. We considered *data–model* approach to generate this profile, where the model represents the best fit straight line at the two different velocity gradient regimes. It has been suggested that the large-scale velocity oscillations in the pv diagram along the filaments may be related to the kinematics of core formation and to the physical os-

cillations present in the filaments (e.g., Liu et al. 2019, see Figure 7 therein).

In order to compare the velocity oscillations with the column density enhancements in the observed molecular cloud, we have produced the column density profile along a path as shown by a dashed (red) curve in Figure 4a. Figure 7c shows such column density profile, where the zero point in the x-axis corresponds to the eastern end of the path (see Figure 4a). In this exercise, we have used *Herschel* multiwavelength images at 160–500 μ m to obtain the column density map (37'' resolution) of our target area. The details of the adopted procedure can be found in Dewangan et al. (2017c). To make a consistent comparison between velocity and column density plots, we convolved both the data (i.e., ¹³CO(1–0) molecular line data and *Herschel* column density map) into the same spatial resolution of 38''. In this exercise we used CASA¹ based task *imsmooth*. The plots presented in Figure 7 are derived at 38'' spatial resolution. In Figure 7, we marked vertical dashed lines across all the plots, specifying the positions of local column density peaks. From the comparison of velocity and column density plots (Figures 7a and 7c), we note that the velocity peaks are shifted with respect to column density peaks in the direction of G45E. However, this is not obvious in the other parts of the filaments. The possible outcomes from this analysis are discussed in Section 4.1.

3.2. Physical properties of the cloud associated with G45E and G45W

To derive the mass of the filamentary cloud at [53, 63] km s⁻¹, we have employed the ¹³CO(1–0) line emission. Considering local thermodynamical equilibrium (LTE), one can estimate the ¹³CO(1–0) column density ($N(^{13}\text{CO})$) using the following equation (e.g., Garden et al. 1991; Bourke et al. 1997; Mangum & Shirley 2015)

$$N(^{13}\text{CO}) = 2.42 \times 10^{14} \frac{T_{\text{ex}} + 0.88}{1 - \exp(-5.29/T_{\text{ex}})} \int \tau_{13} dv, \quad (1)$$

where τ_{13} is the optical depth of ¹³CO(1–0), T_{ex} is the mean excitation temperature, and v is the local standard of rest (LSR) velocity measured in km s⁻¹. Since the ¹²CO(1–0) emission is optically thick, one can calculate

¹ <https://casa.nrao.edu/>

the T_{ex} using $^{12}\text{CO}(1-0)$ as follows (Garden et al. 1991; Xu et al. 2018)

$$T_{\text{ex}} = \frac{5.53}{\ln \left[1 + \frac{5.53}{T_{\text{mb}}(^{12}\text{CO}) + 0.82} \right]}, \quad (2)$$

where T_{mb} is the main-beam brightness temperature. Figure 8a presents the excitation temperature map of $^{12}\text{CO}(1-0)$ emission. The estimated mean excitation temperature is about 8.7 K. Here, one can assume that the excitation temperatures of $^{12}\text{CO}(1-0)$ and $^{13}\text{CO}(1-0)$ are the same for the entire cloud. We can then derive optical depth (τ) using the equation (Garden et al. 1991; Xu et al. 2018)

$$\tau(^{13}\text{CO}) = -\ln \left[1 - \frac{T_{\text{mb}}(^{13}\text{CO})}{\frac{5.29}{\exp(5.29/T_{\text{ex}}) - 1} - 0.89} \right] \quad (3)$$

The optical depth map of $^{13}\text{CO}(1-0)$ is shown in Figure 8b. We found that the optical depth ranges from ~ 0.1 to 1, suggesting the optically thin nature of the ^{13}CO emission toward the entire filamentary cloud. Using Equations 1, 2, and 3, we have obtained the average value of $N(^{13}\text{CO})$ around $2.04 \times 10^{16} \text{ cm}^{-2}$. This leads to the mean H_2 column density ($N(\text{H}_2)$) of $\sim 1.43 \times 10^{22} \text{ cm}^{-2}$ after adopting the column density conversion factor $N(\text{H}_2)/N(^{13}\text{CO}) \simeq 7 \times 10^5$ from Frerking et al. (1982). In this calculation, we considered the emission inside the filamentary cloud by adopting the minimum $N(^{13}\text{CO})$ emission value of $8 \times 10^{15} \text{ cm}^{-2}$. The derived $N(\text{H}_2)$ map is shown in Figure 8c. Here, we also note that the $N(\text{H}_2)$ maps derived from the *Herschel* continuum images and the molecular line data are consistent with each other. We have calculated the mass of the filamentary cloud using the relation of mass and H_2 column density as given in Equation 1 of Bhadari et al. (2020). In this calculation, we considered the mean molecular weight of 2.8, and the distance of 8 kpc. The total estimated mass of the cloud is $\sim 1.1 \times 10^6 M_{\odot}$. We note that the uncertainties in column density and mass calculations are primarily due to choice of $N(\text{H}_2)/N(^{13}\text{CO})$ factor, distance estimation, and the observational random errors, which can contribute to 30–50% uncertainty. We have also estimated the length of the filamentary cloud to be about 75 pc, which is measured along its long axis (see a dashed (red) curve in Figure 4a). The observed line mass of the cloud is then estimated to be $\sim 1.5 \times 10^4 M_{\odot}/\text{pc}$. The line mass of the filament depends upon the “ $\cos i$ ” factor, where “ i ” is an angle between the sky plane and the major axis of the filament. In our calculations, we assume $i=0$ (i.e., the filament is in the sky plane); hence the derived value represents an

upper limit. However, in addition to the uncertainty in “ i ”, the line mass is mainly affected by the uncertainty in distance estimation, which is about 20–30% (see Section 1).

To assess the gravitational instability of the filamentary cloud, one can compare the observed line mass with the virial line mass. The virial line mass contains the effect of gas turbulence helping the filament to resist the collapse due to gravity. Following the Equation 2 of Dewangan et al. (2019), the virial line mass of the entire cloud is found to be $\sim 4.5 \times 10^3 M_{\odot}/\text{pc}$. In the virial line mass calculation, we considered the expression of non-thermal velocity dispersion (σ_{NT}) as defined in the Equation 3 of Bhadari et al. (2020), where the observed linewidth (ΔV) of $^{13}\text{CO}(1-0)$ spectra is used as 6.8 km s^{-1} , and the gas kinetic temperature (T_{K}) of 18 K. The ΔV and T_{K} values are obtained from the Gaussian fitting of averaged $^{13}\text{CO}(1-0)$ spectra and the dust temperature map for the entire cloud region, respectively. We have also calculated the line mass parameters of the central region (size $\sim 0^{\circ}.29 \times 0^{\circ}.056$; position angle = 13° ; $l = 45^{\circ}.29$, $b = 0^{\circ}.109$) of the cloud. Concerning to the central region, the observed line mass and the virial line mass are estimated to be $\frac{3.24 \times 10^4 M_{\odot}}{40 \text{ pc}} \simeq 800 M_{\odot}/\text{pc}$ and $\sim 3.5 \times 10^3 M_{\odot}/\text{pc}$, respectively. Here, the calculation uses $T_{\text{K}} = 18 \text{ K}$ and $\Delta V = 6 \text{ km s}^{-1}$. We note that the uncertainties in these analyses may be relatively high ($\geq 50\%$) due to distance uncertainty, an unknown inclination of the filament, and the derived ΔV and T_{K} values. The non-thermal velocity dispersion derived from ΔV could be overestimated due to the optical depth effect and multicomponent structure of the $^{13}\text{CO}(1-0)$ line. The implications of these results are discussed in Section 4.1.

3.3. Identification and Distribution of YSOs

The presence of young stellar objects (YSOs) or infrared excess sources in any star-forming region is indicative of ongoing star formation activity. The origin of infrared emission (in excess) is explained by the radiative reprocessing of starlight by the thick circumstellar material (e.g., envelope, disk) around them. In order to identify the YSOs, we have utilized the photometric data at NIR-MIR wavelengths (1–24 μm), which are obtained from different infrared surveys (e.g., UKIDSS-GPS, 2MASS, GLIMPSE, and MIPS GAL). The YSOs towards the target region of our study are identified using the color-color and color-magnitude diagrams.

We obtained the photometric magnitudes of point-like objects at 3.6, 4.5, and 5.8 μm wavelengths from the *Spitzer* GLIMPSE-I Spring’ 07 highly reliable catalog. In this selection, we considered only objects with a pho-

tometric error of less than 0.2 mag in the selected *Spitzer* bands. Figure 9a shows the color-color plot ($[4.5]-[5.8]$ vs. $[3.6]-[4.5]$) of point-like objects toward our line of sight. We followed the infrared color conditions of $[4.5]-[5.8] \geq 0.7$ mag and $[3.6]-[4.5] \geq 0.7$ mag from previous works of Hartmann et al. (2005) and Getman et al. (2007), and this selection provided us a sample of Class I YSOs in the extended physical system. A total of 55 Class I YSOs are identified using this scheme, which are shown by open red circles in Figure 9a.

We have also utilized the photometric data at *Spitzer* 3.6 and 24 μm to identify the different classes of YSOs. Earlier, Guieu et al. (2010) used a color-magnitude plot of $[3.6]-[24]$ vs. $[3.6]$ to distinguish different classes of YSOs along with the possible contaminant sources (e.g., galaxies, diskless stars). Using this scheme, we have identified a total of 87 YSOs (29 Class I, 25 Flat spectrum, and 33 Class II). The color-magnitude plot of $[3.6]-[24]$ vs. $[3.6]$ is shown in Figure 9b, where the Class I, Flat spectrum, and Class II sources are indicated by red circles, green diamonds, and blue triangles, respectively.

Additional color excess sources are also obtained from the color-magnitude diagram of $H - K$ vs. K (see Figure 9c). A large number of 1486 color excess sources (marked by green dots) are identified following the color cutoff condition of $H - K > 1.65$. This condition is decided based upon the upper limit of $H - K$ detection of main sequence stars in the nearby control field. Altogether, after taking account of the common sources identified from different schemes, a total of 1628 YSO candidate sources are identified toward our selected target area. The positions of all the YSOs are presented in Figure 10a.

We have also performed the surface density analysis of all the selected YSO candidates using the nearest neighbour (NN) method (e.g., Gutermuth et al. 2009). To generate the surface density map, we considered a grid size of $15''$ and the 6 NN YSOs at the distance of 8 kpc (see formalism in Casertano & Hut 1985). Figure 10b presents the overlay of surface density contours (in red) on the $^{13}\text{CO}(1-0)$ integrated intensity map. The surface density distribution is primarily concentrated at the positions of G45E and G45W.

3.4. Structure of the dense gas and hub-filament systems

We have used $^{13}\text{CO}(3-2)$ line data to trace the morphology and kinematics of dense gas. The velocity channel maps of $^{13}\text{CO}(3-2)$ emission in the direction of G45W are shown in Figure 11. We have overlaid the velocity averaged emission (at each 1 km interval;

see contours) on the $^{13}\text{CO}(1-0)$ moment-0 map. This exercise allows us to identify the dense gas structures, which are highly elongated/filamentary as seen in the velocity range from 55.59 km s^{-1} to 61.59 km s^{-1} . The elongated gas structures are extended to the locations of both the IRAS sources (i.e., IRAS 19110+1045 and IRAS 19111+1048). The last two panels of the channel maps present the moment-0 and moment-1 maps of the $^{13}\text{CO}(3-2)$ emission, which are obtained for the velocity range as presented in the channel maps (i.e., $[52.59, 64.59] \text{ km s}^{-1}$). From the moment maps, the presence of elongated structures and the velocity gradient along them are evident.

Based on the visual inspection of Figure 2a, we can notice the possible presence of filamentary structures (sub-filaments) in our target site. To further explore these structures, we have used *getsf*, a newly developed tool for extraction of sources and filaments in astronomical images (Men'shchikov 2021). The *getsf* spatially decomposes the image into its structural components and separates them from each other and from their backgrounds. After flattening the residual noise in the resulting images, it decomposes the flattened images and identifies the positions of sources and skeletons of filaments. To identify structures using *getsf*, it requires a single user-defined input i.e., the maximum size of the structure to be extracted (e.g., filaments in our case).

Figure 12 presents the *getsf* identified filament skeletons (on global scale) in our target site. We have used the *Herschel* continuum images at 160 μm and 250 μm to identify the subfilaments. Figure 12a shows the *Herschel* 160 μm filament skeletons identified on the image scales of $12''$ - $543''$. Figure 12b displays the *Herschel* 250 μm filament skeletons identified on the scales of $18''$ - $576''$. In order to trace the genuine subfilaments in a star-forming site, one should also look for filaments in molecular line emission apart from the continuum maps. The *getsf* procedure is also applied to the CHIMPS $^{13}\text{CO}(3-2)$ moment-0 map ($V_{\text{lsr}} \sim 53$ - 66 km s^{-1} , $\theta_{\text{spatial}}=15''$). In Figure 12c, the *getsf* identified filaments on the scales of $15''$ - $679''$ are highlighted on the CHIMPS $^{13}\text{CO}(3-2)$ moment-0 map. In the whole exercise, the input parameter of maximum width (FWHM, in arcsec) of filaments to be extracted was used as $260''$, $420''$, and $400''$ for the *Herschel* 160 μm , the *Herschel* 250 μm , and the CHIMPS $^{13}\text{CO}(3-2)$ emission maps, respectively.

From the comparison of maps displayed in Figure 12, we notice that the filamentary structures in the direction of dense regions (i.e., high intensity regions) are consistent with the structures seen in the continuum and molecular emission maps, thus revealing the potential subfilaments in our target sites. It is interest-

ing to note that the structures of subfilaments in sites G45E and G45W are the reminiscences of HFSs (see Section 1). The hub-filament configurations are clearly evident in both the complexes (i.e., toward G45E and G45W), which are primarily associated with the previously known massive star-forming sites (i.e., IRAS sources; see Figure 12a). These outcomes are further discussed in Section 4.2.

4. DISCUSSION

4.1. End dominated collapse in a giant molecular filament GMF G45.3+0.1

In Section 3.1, we have investigated that the sites G45E and G45W are part of a filamentary cloud (see also Section 1), and are located at the ends of it. Based on the physical length of 75 pc and the derived mass of $\sim 1.1 \times 10^6 M_\odot$ (see Section 3.2), the cloud can be considered as a giant molecular cloud (GMC; Solomon et al. 1987). Hence, considering the position in the Galactic system, we named this filamentary cloud as a giant molecular filament (GMF) G45.3+0.1. However, previously the eastern part of GMF G45.3+0.1 (i.e., G45E) was itself considered to be a large filament and cataloged as “F39” by Wang et al. (2016, see Figure 6 therein). Zhang et al. (2019) further included the western part of GMF G45.3+0.1 (i.e., G45W) and cataloged the entire filament as “GMF 37”. The clear definition of a GMF is not available in the literature. However, according to Zhang et al. (2019), one must see a clear elongation in the cloud over some column-density regime, and the cloud should show coherence in the position-position-velocity (PPV) space. The GMFs have lengths of the order of ~ 100 pc and masses of $\sim 10^3$ – $10^6 M_\odot$ (e.g., Li et al. 2013; Ragan et al. 2014; Su et al. 2015; Abreu-Vicente et al. 2016; Zhang et al. 2019). Adopting a typical cloud width range of ~ 8 – 10 pc, which can vary along the major axis of the cloud because of its evolution in terms of structure, shaped by the feedback from embedded stars (e.g., McKee & Ostriker 2007), the GMF G45.3+0.1, always have a high aspect ratio ($A \sim 7$ – 10 ; i.e., a ratio of filament’s length to diameter). Such high aspect ratio ($A > 5$) filaments are considered to collapse at the edges due to the gravitational instability induced by the high gas acceleration (Bastien 1983; Pon et al. 2012; Clarke & Whitworth 2015; Hoemann et al. 2022).

Till now, very few observational examples of filaments showing end-dominated collapse are available in the literature, which include NGC 6334 (Zernickel et al. 2013), IRDC 18223 (Beuther et al. 2015), Musca cloud (Kainulainen et al. 2016), S242 (Dewangan et al. 2017a, 2019), G341.244–00.265 (Yu et al. 2019), and Mono-

ceros R1 (Bhadari et al. 2020). The key features of such physical process include at least one of the following possibilities i.e., the existence of high column density clumps, star clusters, and HII regions at one or both the filament ends. Such filaments should ideally be observed as isolated clouds in 3D or position-position-position (PPP) space. However, these filaments are generally identified as coherent velocity clouds in the PPV space. Theoretically, there is no restriction on the filament’s parameter (i.e., length or radius) for it to collapse by the end-dominated process; instead, the global collapse of filament (specifically, the collapse timescale) is dependent on the aspect ratio (e.g., Toalá et al. 2012; Pon et al. 2012; Clarke & Whitworth 2015). In Section 3.2, we found that the observed line mass of GMF G45.3+0.1 is larger than the virial line mass, suggesting that it is gravitationally unstable and prone to collapse. However, the central region of GMF G45.3+0.1, where the star formation activity is not dominated, shows the opposite nature. Previously, Dewangan et al. (2019) also found that the central region of S242 filament shows higher virial mass compared to the observed line mass. This suggests that the cloud is self-gravitating and gravitational unstable at the edges compared to the central areas.

Based on our observational outcomes, we argue that the global collapse of GMF G45.3+0.1 is predominately end-dominated in nature. This argument is supported by the fact that the sites G45E and G45W are observed at the ends of GMF G45.3+0.1, where a large number of YSO clusterings and the presence of HII regions are also observed. The major column density peaks are also seen at the ends of GMF G45.3+0.1 (Figure 7c). We also note that the complex G45E is more extended than the G45W. It is probably possible because of the rapid structural evolution of G45E from the feedback of embedded stars.

The fragmentation of GMF G45.3+0.1 appears to proceed in a hierarchy (i.e., into subfilaments) as seen in the dense gas site G45W. In the direction of complex G45W, the ATLASGAL map at $870 \mu\text{m}$ shows the presence of a filamentary structure (length ~ 12 pc; see Figure 2c) connecting the two massive star-forming sites, IRAS 19110+1045 and IRAS 19111+1048. This subfilament is found to be denser than the parent filament, as it is traced in the relatively dense gas tracers of $^{13}\text{CO}/\text{C}^{18}\text{O}(3-2)$ emission (see Figures 4b, 11), thus indicating the hierarchical fragmentation of GMF G45.3+0.1. Some previous observational (e.g., Hacar et al. 2013; Tafalla & Hacar 2015; Hacar et al. 2018) and theoretical (e.g., Smith et al. 2016; Clarke et al. 2017,

2020) works also favor the hierarchical fragmentation of filaments. These results significantly deviate from previous models of filament fragmentation which favour the formation of quasi-periodically spaced cores along filaments (e.g., Inutsuka & Miyama 1992, 1997; Fischera & Martin 2012). Clarke et al. (2020) argue that the hierarchical fragmentation of filaments diminishes the signature of characteristic fragmentation length-scale (related to the quasi-periodically spaced cores), and the cores are formed by the fragmentation of subfilaments rather than the main filament itself. We observed oscillations in the mean velocity profile along the long axis of GMF G45.3+0.1 (see Figures 6c and 7), which hints the signature of core formation (e.g., Beuther et al. 2015; Kainulainen et al. 2016) together with the possibility of large scale physical oscillations in the filament (Liu et al. 2019). However, based on the comparison of velocity and column density plots (Figure 7), we observed that the column density and velocity peaks toward G45E are shifted with respect to each other. This could be an indication of the presence of gravitationally bound cores (e.g., Hacar & Tafalla 2011, see Figure 12 therein). Some of the other column density peaks along filament do not significantly correlate to the velocity oscillations, suggesting that the cores are not gravitationally bound.

We have observed linear gradients in the velocity profile along the long axis of GMF G45.3+0.1. At the eastern end of the filament (toward G45E), the linear gradient is negative and twice in magnitude to that of the positive gradient toward the western end. The origin of these adverse gradients at the filament's edges can probably be explained by the presence of sites G45E and G45W itself, where the feedback from massive stars in these sites appears to shape the cloud in terms of structure and kinematics.

4.2. Hub-filament systems and star formation scenario

The current understanding of star formation argues that the complex filaments form initially in the molecular clouds (e.g., Chen et al. 2020a; Abe et al. 2021, and references therein), which then undergo the fragmentation processes to form dense clumps/cores and ultimately the stellar clusters (e.g., Hacar et al. 2013). However, despite taking birth in the clustered environment, the formation theories of massive stars ($\geq 8 M_{\odot}$) are still an enigmatic topic of research (e.g., Motte et al. 2018, and references therein). In this context, the necessity of the mass reservoir becomes vital for the formation of massive stars (i.e., massive star formation; MSF), which can be fulfilled in the physical environment of filaments.

In Section 3.4, we found that the star-forming complexes G45E and G45W appear to have the morphology of parsec scale HFSs. These HFSs are primarily investigated in the direction of massive star-forming regions (i.e., IRAS sources; see Figures 2 and 12), and have the filament's length of the order of ~ 5 – 10 pc in the vicinity of IRAS sites. Overall, these filaments show converging networks toward the hubs (or local intensity peaks), where they either direct to the hubs or merge with the other longer spines approaching to hubs. The onset of the edge-collapse process, together with the presence of HFSs in GMF G45.3+0.1, is quite intriguing, hence opens up a new possibility of MSF, including the formation of HFSs (e.g., Motte et al. 2018; Wang et al. 2020, and references therein).

The EDC process can well explain the formation of star-forming sites G45E and G45W. However, the presence of HFSs in these sites itself hints the onset of global nonisotropic collapse (GNIC; Tigé et al. 2017; Motte et al. 2018; Treviño-Morales et al. 2019). GNIC scenario supports the mass accretion onto the dense core from the large scale structures. In this paradigm, a density-enhanced hub hosts massive dense cores (MDCs; size ~ 0.1 pc), which in their starless phase harbor low-mass prestellar cores. Later, MDCs become protostellar, hosting only low-mass stellar embryos, which grow into high-mass protostars from gravitationally-driven inflows (see more details in Motte et al. 2018). Observational studies of HFSs report that the longitudinal flow rate along filaments is around 10^{-4} – $10^{-3} M_{\odot} \text{ year}^{-1}$ (e.g., Kirk et al. 2013; Chen et al. 2019; Treviño-Morales et al. 2019) which is a close value to the sufficient inflow rate for MSF (e.g., Haemmerlé et al. 2016, and references therein). Hence, it is now believed that all massive stars favour forming in the density-enhanced hubs of HFSs (e.g., Motte et al. 2018; Anderson et al. 2021, and references therein). It has also been thought that the onset of collision process (see the review article by Fukui et al. 2021, and references therein) can produce hubs with large networks of filaments. The filamentary structures, reminiscent of the HFSs are quite evident in the smoothed particle hydrodynamics simulations of two colliding clouds (Balfour et al. 2015). In this case, the shock-compressed layer is found to fragment into filaments. Furthermore, the pattern of filaments appears to have the morphology of HFSs, spider's web, and spokes system (Balfour et al. 2015).

Recently, Clarke et al. (2020) found that the filaments are more prone to fragment into subfilaments, and these subfilaments are responsible for the formation of hubs via their merging event. Also, the cores which are

formed at the filament's edges are more massive than the interior ones (Clarke et al. 2020). Thus, one can argue that the HFSs seen in a giant molecular filament are possibly formed by the combined effect of colliding subfilaments and the fragmentation of shock-compressed layers in the collision sites. Comparing all these theoretical results with our observational outcomes of the study of GMF G45.3+0.1, we argue that the star formation activity in G45E and G45W, primarily proceed through the onset of EDC and HFSs. We notice that the HFSs are preferentially formed at the edges of GMF G45.3+0.1, where massive end clumps are also expected from the EDC process. All our observations are constrained by the limited resolution of the existing data, which for a large source distance of our target site (8 kpc for GMF G45.3+0.1), make it further intricate.

Thus, our observational outcomes reveal GMF G45.3+0.1 as an observational sample of filament, identified so far in the interstellar medium, where the edge collapse and the hub-filament configurations are simultaneously seen. Our observational results are more or less consistent with the outcomes from the numerical fragmentation study on filaments by Clarke et al. (2020). Such a study also helps us to understand the formation of HFSs and MSF.

5. SUMMARY AND CONCLUSIONS

This paper is aimed to get new insights into the physical processes operating in the sites G45E and G45W, which are part of a large cloud complex in the Aquila constellation ($l=45^\circ$, $b=0^\circ$). We have performed the analysis of multiwavelength and multiscale data-sets toward an area ($0^\circ.67 \times 0^\circ.50$) enclosing our target sites. The major outcomes from our observational study can be summarized as follows:

1. The analysis of $^{13}\text{CO}(1-0)$ line data reveals the presence of a filamentary cloud (length ~ 75 pc) in the velocity range of $\sim 53-63$ km s $^{-1}$ having the mean velocity and standard deviation of 58.30 ± 0.03 km s $^{-1}$ and 2.34 ± 0.03 km s $^{-1}$, respectively.
2. Using $^{13}\text{CO}(1-0)$ emission maps, the cloud mass is derived to be $\sim 1.1 \times 10^6$ M $_{\odot}$, which further results in the line mass of $\sim 1.5 \times 10^4$ M $_{\odot}$ /pc. Our study thus uncovers a new giant molecular filament, which we named GMF G45.3+0.1.
3. The sites G45E and G45W are observed at the opposite ends of GMF G45.3+0.1. The clustering of YSOs is primarily focused at both ends of the filament, where the presence of HII regions and previously known massive star-forming sites are also observed.
4. The pv diagram along the major axis of GMF G45.3+0.1 shows the velocity oscillations, which could be originated by the combined effect of fragment/core formation and the physical oscillation in the filament. The velocity gradient at both ends of the filament is found to be opposite in sign, i.e., -0.064 km s $^{-1}$ pc $^{-1}$ toward G45E and $+0.032$ km s $^{-1}$ pc $^{-1}$ in the direction of G45W.
5. The sites IRAS 19110+1045 and IRAS 19111+1048, located in G45W, are primarily observed to be a part of ~ 12 pc long dense subfilament. This presents strong evidence of hierarchical fragmentation of GMF G45.3+0.1.
6. The analysis of the dust continuum and molecular line data suggests that both the complexes (G45E and G45W) are associated with the HFSs, where several parsec scale filaments ($\sim 5-10$ pc) appear to converge toward dense regions (i.e., hubs). These hubs are identified in the direction of massive star-forming sites (i.e., IRAS 19120+1103, IRAS 19117+1107, IRAS 19110+1045, and IRAS 19111+1048).

Overall, our observational results suggest that the star-forming complexes in the GMF G45.3+0.1 are formed through the edge collapse scenario and the mass accumulation is evident in each hub through the gas flows along filaments.

ACKNOWLEDGEMENTS

We thank the referee for valuable comments and suggestions that helped improve the paper's presentation. The research work at Physical Research Laboratory is funded by the Department of Space, Government of India. DKO acknowledges the support of the Department of Atomic Energy, Government of India, under Project Identification No. RTI 4002. LEP acknowledges the support of the IAP State Program 0030-2021-0005. NKB thanks Peter Zemlyanukha for helping in the cloud mass calculation using molecular line data. NKB extends heartfelt gratitude to Alexander Men'shchikov for the discussion on the *getsf* tool and its outputs. This work is based on data obtained as part of the UKIRT Infrared Deep Sky Survey. This publication makes use of data products from the Two Micron All Sky Survey, which is a joint project of the University of Massachusetts and the Infrared Processing and Analysis Center/California Institute of Technology, funded by NASA and NSF. This work is based [in part] on

observations made with the *Spitzer* Space Telescope, which is operated by the Jet Propulsion Laboratory, California Institute of Technology under a contract with

NASA. This publication makes use of data from FUGIN, FOREST Unbiased Galactic plane Imaging survey with the Nobeyama 45-m telescope, a legacy project in the Nobeyama 45-m radio telescope.

REFERENCES

- Abe, D., Inoue, T., Inutsuka, S.-i., & Matsumoto, T. 2021, *ApJ*, 916, 83, doi: [10.3847/1538-4357/ac07a1](https://doi.org/10.3847/1538-4357/ac07a1)
- Abreu-Vicente, J., Ragan, S., Kainulainen, J., et al. 2016, *A&A*, 590, A131, doi: [10.1051/0004-6361/201527674](https://doi.org/10.1051/0004-6361/201527674)
- Anderson, M., Peretto, N., Ragan, S. E., et al. 2021, *MNRAS*, doi: [10.1093/mnras/stab2674](https://doi.org/10.1093/mnras/stab2674)
- André, P., Men'shchikov, A., Bontemps, S., et al. 2010, *A&A*, 518, L102, doi: [10.1051/0004-6361/201014666](https://doi.org/10.1051/0004-6361/201014666)
- Balfour, S. K., Whitworth, A. P., Hubber, D. A., & Jaffa, S. E. 2015, *MNRAS*, 453, 2471, doi: [10.1093/mnras/stv1772](https://doi.org/10.1093/mnras/stv1772)
- Bastien, P. 1983, *A&A*, 119, 109
- Benjamin, R. A., Churchwell, E., Babler, B. L., et al. 2003, *PASP*, 115, 953, doi: [10.1086/376696](https://doi.org/10.1086/376696)
- Beuther, H., Ragan, S. E., Johnston, K., et al. 2015, *A&A*, 584, A67, doi: [10.1051/0004-6361/201527108](https://doi.org/10.1051/0004-6361/201527108)
- Bhadari, N. K., Dewangan, L. K., Pirogov, L. E., & Ojha, D. K. 2020, *ApJ*, 899, 167, doi: [10.3847/1538-4357/aba2c6](https://doi.org/10.3847/1538-4357/aba2c6)
- Blum, R. D., & McGregor, P. J. 2008, *AJ*, 135, 1708, doi: [10.1088/0004-6256/135/5/1708](https://doi.org/10.1088/0004-6256/135/5/1708)
- Bourke, T. L., Garay, G., Lehtinen, K. K., et al. 1997, *ApJ*, 476, 781, doi: [10.1086/303642](https://doi.org/10.1086/303642)
- Carey, S. J., Noriega-Crespo, A., Price, S. D., et al. 2005, in *American Astronomical Society Meeting Abstracts*, Vol. 207, American Astronomical Society Meeting Abstracts, 63.33
- Casertano, S., & Hut, P. 1985, *ApJ*, 298, 80, doi: [10.1086/163589](https://doi.org/10.1086/163589)
- Chen, C.-Y., Mundy, L. G., Ostriker, E. C., Storm, S., & Dhabal, A. 2020a, *MNRAS*, 494, 3675, doi: [10.1093/mnras/staa960](https://doi.org/10.1093/mnras/staa960)
- Chen, H.-R. V., Zhang, Q., Wright, M. C. H., et al. 2019, *ApJ*, 875, 24, doi: [10.3847/1538-4357/ab0f3e](https://doi.org/10.3847/1538-4357/ab0f3e)
- Chen, M. C.-Y., Di Francesco, J., Rosolowsky, E., et al. 2020b, *ApJ*, 891, 84, doi: [10.3847/1538-4357/ab7378](https://doi.org/10.3847/1538-4357/ab7378)
- Clarke, S. D., & Whitworth, A. P. 2015, *MNRAS*, 449, 1819, doi: [10.1093/mnras/stv393](https://doi.org/10.1093/mnras/stv393)
- Clarke, S. D., Whitworth, A. P., Duarte-Cabral, A., & Hubber, D. A. 2017, *MNRAS*, 468, 2489, doi: [10.1093/mnras/stx637](https://doi.org/10.1093/mnras/stx637)
- Clarke, S. D., Williams, G. M., & Walch, S. 2020, *MNRAS*, 497, 4390, doi: [10.1093/mnras/staa2298](https://doi.org/10.1093/mnras/staa2298)
- Dewangan, L. K. 2021, *MNRAS*, 504, 1152, doi: [10.1093/mnras/stab1008](https://doi.org/10.1093/mnras/stab1008)
- Dewangan, L. K., Baug, T., Ojha, D. K., et al. 2017a, *ApJ*, 845, 34, doi: [10.3847/1538-4357/aa7da2](https://doi.org/10.3847/1538-4357/aa7da2)
- Dewangan, L. K., Ojha, D. K., & Baug, T. 2017b, *ApJ*, 844, 15, doi: [10.3847/1538-4357/aa79a5](https://doi.org/10.3847/1538-4357/aa79a5)
- Dewangan, L. K., Ojha, D. K., Sharma, S., et al. 2020, *ApJ*, 903, 13, doi: [10.3847/1538-4357/abb827](https://doi.org/10.3847/1538-4357/abb827)
- Dewangan, L. K., Ojha, D. K., & Zinchenko, I. 2017c, *ApJ*, 851, 140, doi: [10.3847/1538-4357/aa9be2](https://doi.org/10.3847/1538-4357/aa9be2)
- Dewangan, L. K., Pirogov, L. E., Ryabukhina, O. L., Ojha, D. K., & Zinchenko, I. 2019, *ApJ*, 877, 1, doi: [10.3847/1538-4357/ab1aa6](https://doi.org/10.3847/1538-4357/ab1aa6)
- Dewangan, L. K., Zinchenko, I. I., Zemlyanukha, P. M., et al. 2022, *ApJ*, 925, 41, doi: [10.3847/1538-4357/ac36dd](https://doi.org/10.3847/1538-4357/ac36dd)
- Fischera, J., & Martin, P. G. 2012, *A&A*, 542, A77, doi: [10.1051/0004-6361/201218961](https://doi.org/10.1051/0004-6361/201218961)
- Frerking, M. A., Langer, W. D., & Wilson, R. W. 1982, *ApJ*, 262, 590, doi: [10.1086/160451](https://doi.org/10.1086/160451)
- Fukui, Y., Habe, A., Inoue, T., Enokiya, R., & Tachihara, K. 2021, *PASJ*, 73, S1, doi: [10.1093/pasj/psaa103](https://doi.org/10.1093/pasj/psaa103)
- Garden, R. P., Hayashi, M., Gatley, I., Hasegawa, T., & Kaifu, N. 1991, *ApJ*, 374, 540, doi: [10.1086/170143](https://doi.org/10.1086/170143)
- Getman, K. V., Feigelson, E. D., Garmire, G., Broos, P., & Wang, J. 2007, *ApJ*, 654, 316, doi: [10.1086/509112](https://doi.org/10.1086/509112)
- Guieu, S., Rebull, L. M., Stauffer, J. R., et al. 2010, *ApJ*, 720, 46, doi: [10.1088/0004-637X/720/1/46](https://doi.org/10.1088/0004-637X/720/1/46)
- Gutermuth, R. A., Megeath, S. T., Myers, P. C., et al. 2009, *ApJS*, 184, 18, doi: [10.1088/0067-0049/184/1/18](https://doi.org/10.1088/0067-0049/184/1/18)
- Hacar, A., & Tafalla, M. 2011, *A&A*, 533, A34, doi: [10.1051/0004-6361/201117039](https://doi.org/10.1051/0004-6361/201117039)
- Hacar, A., Tafalla, M., Forbrich, J., et al. 2018, *A&A*, 610, A77, doi: [10.1051/0004-6361/201731894](https://doi.org/10.1051/0004-6361/201731894)
- Hacar, A., Tafalla, M., Kauffmann, J., & Kovács, A. 2013, *A&A*, 554, A55, doi: [10.1051/0004-6361/201220090](https://doi.org/10.1051/0004-6361/201220090)
- Haemmerlé, L., Eggenberger, P., Meynet, G., Maeder, A., & Charbonnel, C. 2016, *A&A*, 585, A65, doi: [10.1051/0004-6361/201527202](https://doi.org/10.1051/0004-6361/201527202)
- Hartmann, L., Megeath, S. T., Allen, L., et al. 2005, *ApJ*, 629, 881, doi: [10.1086/431472](https://doi.org/10.1086/431472)
- Helfand, D. J., Becker, R. H., White, R. L., Fallon, A., & Tuttle, S. 2006, *AJ*, 131, 2525, doi: [10.1086/503253](https://doi.org/10.1086/503253)

- Hoemann, E., Heigl, S., & Burkert, A. 2022, arXiv e-prints, arXiv:2203.07002. <https://arxiv.org/abs/2203.07002>
- Hunter, T. R., Phillips, T. G., & Menten, K. M. 1997, *ApJ*, 478, 283, doi: [10.1086/303775](https://doi.org/10.1086/303775)
- Inutsuka, S.-I., & Miyama, S. M. 1992, *ApJ*, 388, 392, doi: [10.1086/171162](https://doi.org/10.1086/171162)
- Inutsuka, S.-i., & Miyama, S. M. 1997, *ApJ*, 480, 681, doi: [10.1086/303982](https://doi.org/10.1086/303982)
- Kainulainen, J., Hacar, A., Alves, J., et al. 2016, *A&A*, 586, A27, doi: [10.1051/0004-6361/201526017](https://doi.org/10.1051/0004-6361/201526017)
- Kirk, H., Myers, P. C., Bourke, T. L., et al. 2013, *ApJ*, 766, 115, doi: [10.1088/0004-637X/766/2/115](https://doi.org/10.1088/0004-637X/766/2/115)
- Lawrence, A., Warren, S. J., Almaini, O., et al. 2007, *MNRAS*, 379, 1599, doi: [10.1111/j.1365-2966.2007.12040.x](https://doi.org/10.1111/j.1365-2966.2007.12040.x)
- Li, G.-X., Wyrowski, F., Menten, K., & Belloche, A. 2013, *A&A*, 559, A34, doi: [10.1051/0004-6361/201322411](https://doi.org/10.1051/0004-6361/201322411)
- Liu, H. B., Jiménez-Serra, I., Ho, P. T. P., et al. 2012, *ApJ*, 756, 10, doi: [10.1088/0004-637X/756/1/10](https://doi.org/10.1088/0004-637X/756/1/10)
- Liu, H.-L., Stutz, A., & Yuan, J.-H. 2019, *MNRAS*, 487, 1259, doi: [10.1093/mnras/stz1340](https://doi.org/10.1093/mnras/stz1340)
- Mangum, J. G., & Shirley, Y. L. 2015, *PASP*, 127, 266, doi: [10.1086/680323](https://doi.org/10.1086/680323)
- McKee, C. F., & Ostriker, E. C. 2007, *ARA&A*, 45, 565, doi: [10.1146/annurev.astro.45.051806.110602](https://doi.org/10.1146/annurev.astro.45.051806.110602)
- Men'shchikov, A. 2021, *A&A*, 649, A89, doi: [10.1051/0004-6361/202039913](https://doi.org/10.1051/0004-6361/202039913)
- Molinari, S., Swinyard, B., Bally, J., et al. 2010, *A&A*, 518, L100, doi: [10.1051/0004-6361/201014659](https://doi.org/10.1051/0004-6361/201014659)
- Motte, F., Bontemps, S., & Louvet, F. 2018, *ARA&A*, 56, 41, doi: [10.1146/annurev-astro-091916-055235](https://doi.org/10.1146/annurev-astro-091916-055235)
- Myers, P. C. 2009, *ApJ*, 700, 1609, doi: [10.1088/0004-637X/700/2/1609](https://doi.org/10.1088/0004-637X/700/2/1609)
- Paron, S., Cichowolski, S., & Ortega, M. E. 2009, *A&A*, 506, 789, doi: [10.1051/0004-6361/200912646](https://doi.org/10.1051/0004-6361/200912646)
- Peretto, N., Fuller, G. A., Duarte-Cabral, A., et al. 2013, *A&A*, 555, A112, doi: [10.1051/0004-6361/201321318](https://doi.org/10.1051/0004-6361/201321318)
- Pon, A., Toalá, J. A., Johnstone, D., et al. 2012, *ApJ*, 756, 145, doi: [10.1088/0004-637X/756/2/145](https://doi.org/10.1088/0004-637X/756/2/145)
- Ragan, S. E., Henning, T., Tackenberg, J., et al. 2014, *A&A*, 568, A73, doi: [10.1051/0004-6361/201423401](https://doi.org/10.1051/0004-6361/201423401)
- Rathborne, J. M., Johnson, A. M., Jackson, J. M., Shah, R. Y., & Simon, R. 2009, *ApJS*, 182, 131, doi: [10.1088/0067-0049/182/1/131](https://doi.org/10.1088/0067-0049/182/1/131)
- Rigby, A. J., Moore, T. J. T., Plume, R., et al. 2016, *MNRAS*, 456, 2885, doi: [10.1093/mnras/stv2808](https://doi.org/10.1093/mnras/stv2808)
- Rivera-Ingraham, A., Ade, P. A. R., Bock, J. J., et al. 2010, *ApJ*, 723, 915, doi: [10.1088/0004-637X/723/1/915](https://doi.org/10.1088/0004-637X/723/1/915)
- Schneider, N., Csengeri, T., Hennemann, M., et al. 2012, *A&A*, 540, L11, doi: [10.1051/0004-6361/201118566](https://doi.org/10.1051/0004-6361/201118566)
- Schuller, F., Menten, K. M., Contreras, Y., et al. 2009, *A&A*, 504, 415, doi: [10.1051/0004-6361/200811568](https://doi.org/10.1051/0004-6361/200811568)
- Skrutskie, M. F., Cutri, R. M., Stiening, R., et al. 2006, *AJ*, 131, 1163, doi: [10.1086/498708](https://doi.org/10.1086/498708)
- Smith, R. J., Glover, S. C. O., Klessen, R. S., & Fuller, G. A. 2016, *MNRAS*, 455, 3640, doi: [10.1093/mnras/stv2559](https://doi.org/10.1093/mnras/stv2559)
- Solomon, P. M., Rivolo, A. R., Barrett, J., & Yahil, A. 1987, *ApJ*, 319, 730, doi: [10.1086/165493](https://doi.org/10.1086/165493)
- Su, Y., Zhang, S., Shao, X., & Yang, J. 2015, *ApJ*, 811, 134, doi: [10.1088/0004-637X/811/2/134](https://doi.org/10.1088/0004-637X/811/2/134)
- Tafalla, M., & Hacar, A. 2015, *A&A*, 574, A104, doi: [10.1051/0004-6361/201424576](https://doi.org/10.1051/0004-6361/201424576)
- Tigé, J., Motte, F., Russeil, D., et al. 2017, *A&A*, 602, A77, doi: [10.1051/0004-6361/201628989](https://doi.org/10.1051/0004-6361/201628989)
- Toalá, J. A., Vázquez-Semadeni, E., & Gómez, G. C. 2012, *ApJ*, 744, 190, doi: [10.1088/0004-637X/744/2/190](https://doi.org/10.1088/0004-637X/744/2/190)
- Treviño-Morales, S. P., Fuente, A., Sánchez-Monge, Á., et al. 2019, *A&A*, 629, A81, doi: [10.1051/0004-6361/201935260](https://doi.org/10.1051/0004-6361/201935260)
- Umemoto, T., Minamidani, T., Kuno, N., et al. 2017, *PASJ*, 69, 78, doi: [10.1093/pasj/psx061](https://doi.org/10.1093/pasj/psx061)
- Urquhart, J. S., König, C., Giannetti, A., et al. 2018, *MNRAS*, 473, 1059, doi: [10.1093/mnras/stx2258](https://doi.org/10.1093/mnras/stx2258)
- Vig, S., Ghosh, S. K., Kulkarni, V. K., Ojha, D. K., & Verma, R. P. 2006, *ApJ*, 637, 400, doi: [10.1086/498389](https://doi.org/10.1086/498389)
- Virtanen, P., Gommers, R., Oliphant, T. E., et al. 2020, *Nature Methods*, 17, 261, doi: [10.1038/s41592-019-0686-2](https://doi.org/10.1038/s41592-019-0686-2)
- Wang, J.-W., Koch, P. M., Galván-Madrid, R., et al. 2020, *ApJ*, 905, 158, doi: [10.3847/1538-4357/abc74e](https://doi.org/10.3847/1538-4357/abc74e)
- Wang, K., Testi, L., Burkert, A., et al. 2016, *ApJS*, 226, 9, doi: [10.3847/0067-0049/226/1/9](https://doi.org/10.3847/0067-0049/226/1/9)
- Wood, D. O. S., & Churchwell, E. 1989, *ApJS*, 69, 831, doi: [10.1086/191329](https://doi.org/10.1086/191329)
- Wright, E. L., Eisenhardt, P. R. M., Mainzer, A. K., et al. 2010, *AJ*, 140, 1868, doi: [10.1088/0004-6256/140/6/1868](https://doi.org/10.1088/0004-6256/140/6/1868)
- Xu, J.-L., Xu, Y., Zhang, C.-P., et al. 2018, *A&A*, 609, A43, doi: [10.1051/0004-6361/201629189](https://doi.org/10.1051/0004-6361/201629189)
- Yu, N.-P., Xu, J.-L., & Wang, J.-J. 2019, *A&A*, 622, A155, doi: [10.1051/0004-6361/201832962](https://doi.org/10.1051/0004-6361/201832962)
- Zernickel, A., Schilke, P., & Smith, R. J. 2013, *A&A*, 554, L2, doi: [10.1051/0004-6361/201321425](https://doi.org/10.1051/0004-6361/201321425)
- Zhang, M., Kainulainen, J., Mattern, M., Fang, M., & Henning, T. 2019, *A&A*, 622, A52, doi: [10.1051/0004-6361/201732400](https://doi.org/10.1051/0004-6361/201732400)

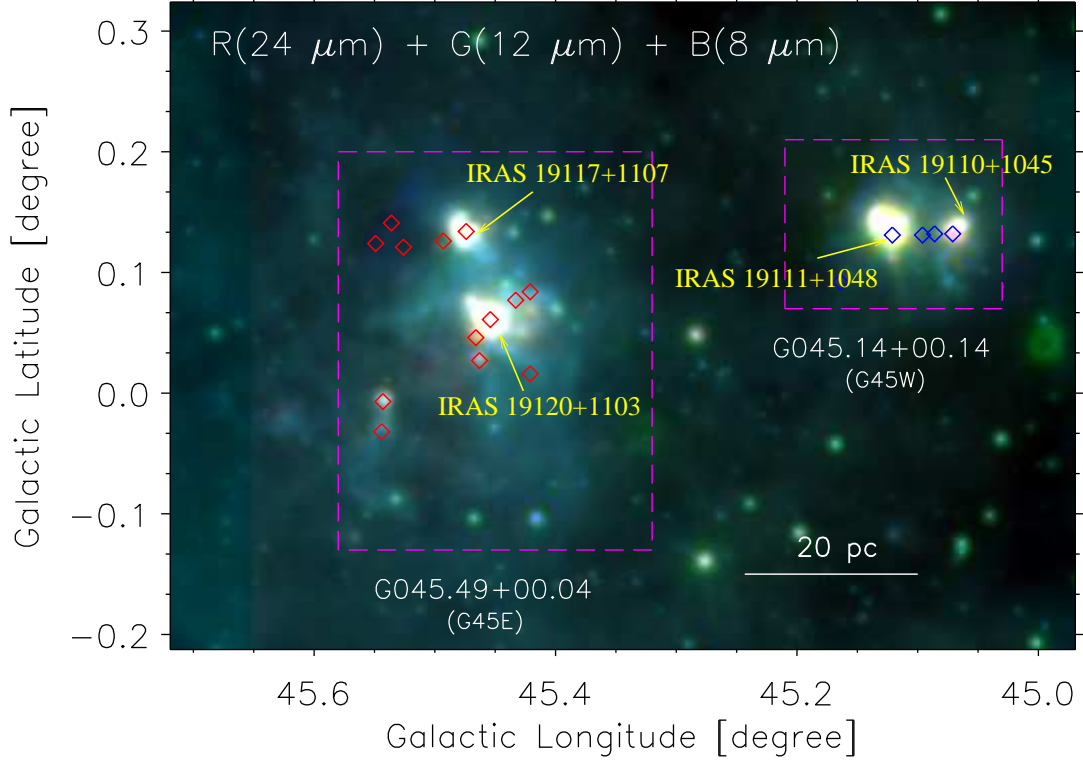


Figure 1. Three-color composite image (Red: *Spitzer* 24 μm , Green: *WISE* 12 μm , Blue: *Spitzer* 8 μm) of a field containing star-forming complexes G045.49+00.04 (G45E) and G045.14+00.14 (G45W). Two dashed rectangular boxes (in magenta) enclose the areas of G45E and G45W (from GRSMC; Rathborne et al. 2009), and are presented in Figures 2b and 2c. The red and blue diamonds represent the positions of ATLASGAL dust clumps at distances of 8.4 kpc and 8.0 kpc, respectively, from Urquhart et al. (2018). The positions of the IRAS sources are shown by arrows. A scale bar of 20 pc (at $d = 8$ kpc) is also displayed.

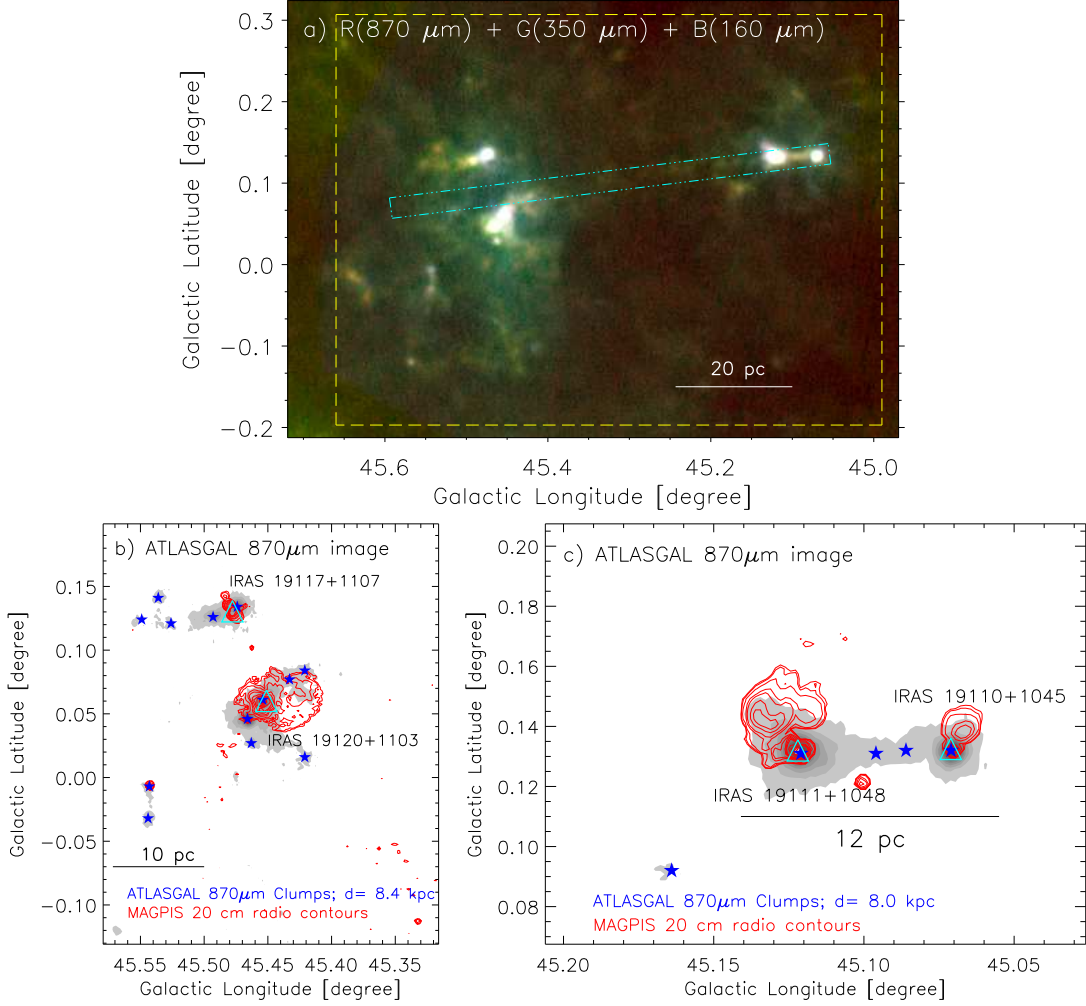


Figure 2. (a) Three-color composite image (Red: ATLASGAL 870 μm , Green: *Herschel* 350 μm , Blue: *Herschel* 160 μm) of a field shown in Figure 1. A dotted dashed rectangular strip (in spring green) indicates an area where the averaged gas spectra are extracted (see Figure 3). A dashed box in yellow highlights an area studied in this work. Panels (b) and (c) display the ATLASGAL dust continuum contour maps (in grey scale) of G045.49+00.04 and G045.14+00.14 regions at 870 μm , respectively (see dashed boxes in Figure 1). In panels (b) and (c), the ATLASGAL contour levels range from 5% to 95% in steps of 9%, of the map peak value (i.e., 5.49(7.56) Jy beam $^{-1}$ for panel “b”(“c”). The maps are overlaid with the MAGPIS 20 cm continuum emission contours with the levels of 0.96, 1.36, 2.73, 8.19, 13.64, 27.29, 40.93, 54.57, 109.15, 163.72, 218.30, 259.23, 267.41 mJy beam $^{-1}$. The star symbols in panels (b) and (c) represent the positions of ATLASGAL dust clumps (see also Figure 1), and the cyan triangles indicate the positions of IRAS sources.

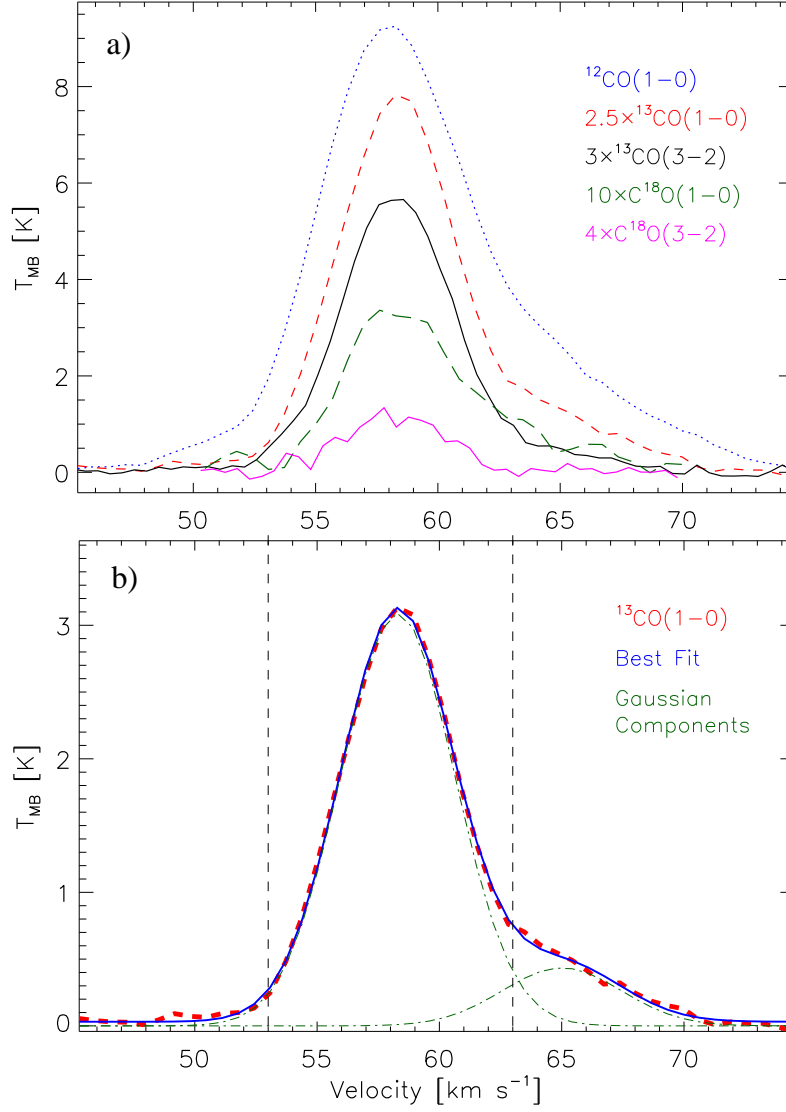


Figure 3. (a) Averaged spectral profiles of different molecular species along the dotted-dashed strip shown in Figure 2a. (b) $^{13}\text{CO}(1-0)$ line profile (dashed (red) curve) fitted with the two Gaussian components (dotted-dashed (green) curves). The best fit profile is shown in a thick blue curve. The two vertical dashed lines are marked at the velocity of 53 and 63 km s^{-1} .

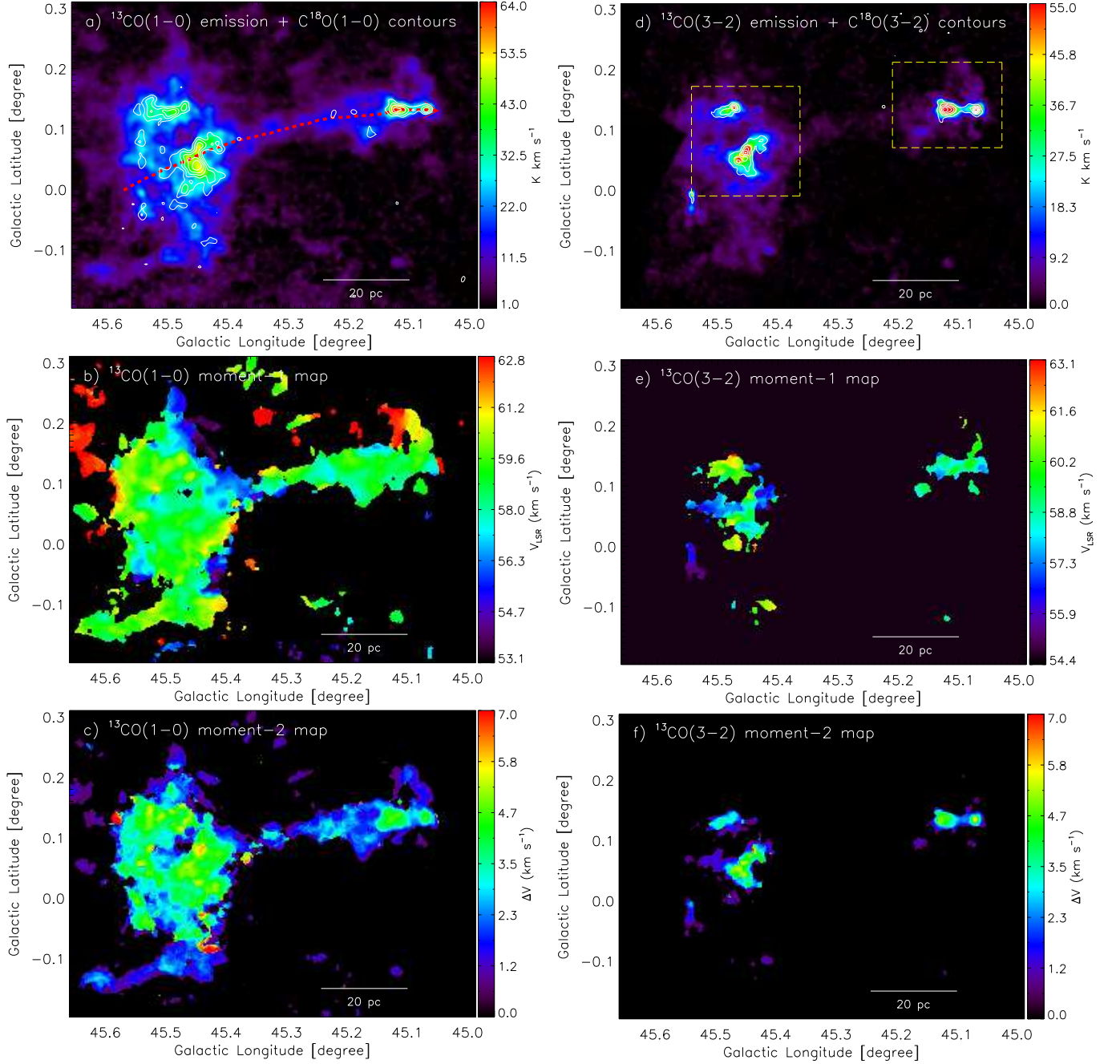


Figure 4. Left column of panels shows the FUGIN $^{13}\text{CO}(1-0)$ moment maps; (a) moment-0 map, (b) moment-1 map, and (c) moment-2 map in the direction of our selected target area (see a dashed box in Figure 2a). Right column of panels shows the similar maps for CHIMPS $^{13}\text{CO}(3-2)$ emission. The moment-0 maps are obtained in the velocity range of $[53, 63] \text{ km s}^{-1}$. In panel (a), $\text{C}^{18}\text{O}(1-0)$ emission contours are overlaid on the $^{13}\text{CO}(1-0)$ moment-0 map. The contour levels range from 3 to 8.7 K km s^{-1} in steps of 1.3 K km s^{-1} . In panel (d), the $\text{C}^{18}\text{O}(3-2)$ emission contours are overlaid with the levels ranging from 3.2 to 20 K km s^{-1} in steps of 3.36 K km s^{-1} . Two dashed boxes in panel (d) show the area presented in Figure 12. In panel (a), a dashed (red) curve is indicative of filament's length, where the position-velocity diagram is also studied (see Figure 6c). In all the panels, the respective color bars are shown to the right of each panel.

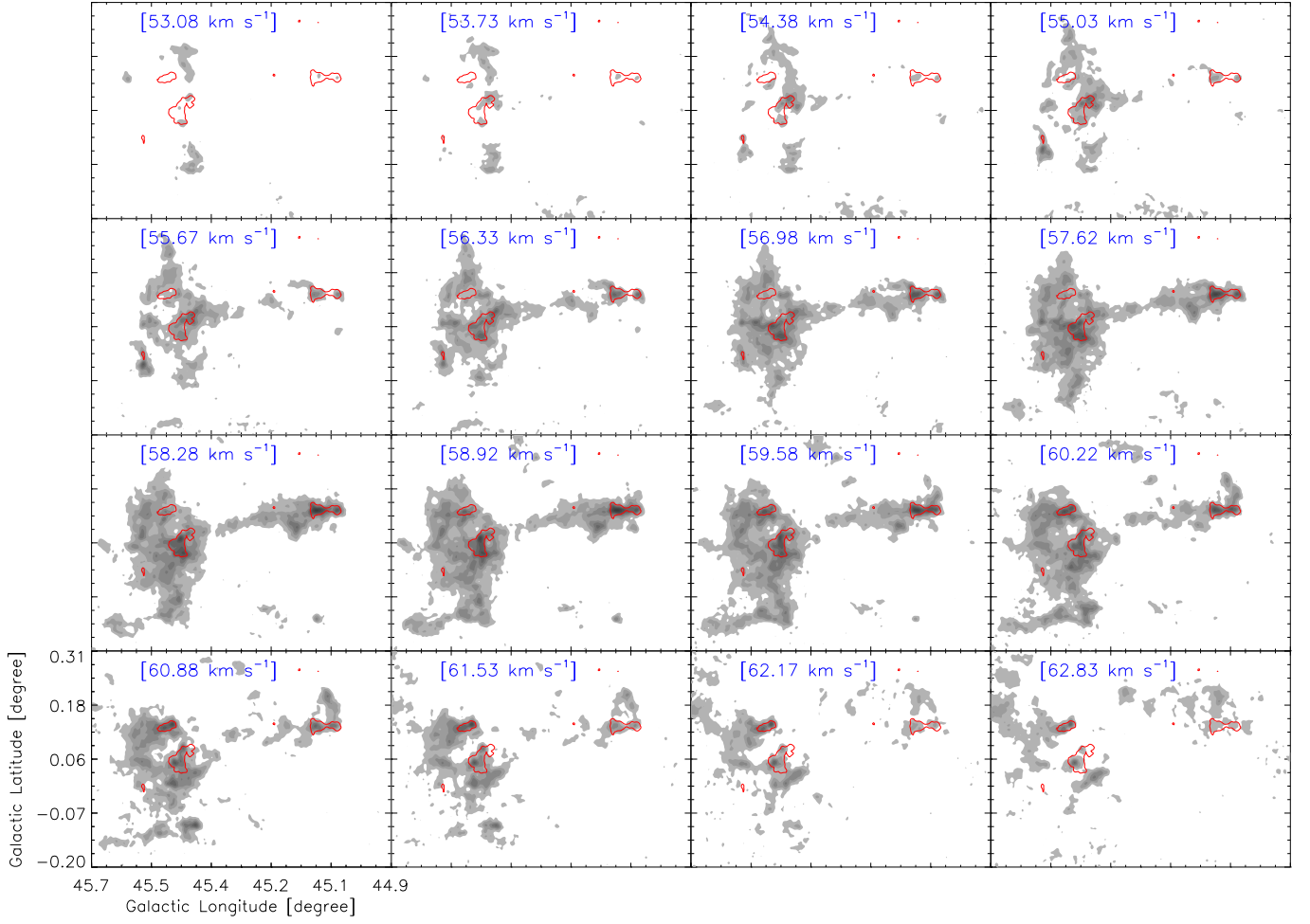


Figure 5. Velocity channel maps of $^{13}\text{CO}(1-0)$ emission (in grayscale). The contour levels range from 1.2 to 14 K in steps of 1.28 K. The overlaid red contours represent the integrated emission of $\text{C}^{18}\text{O}(3-2)$ at a level of 3.2 K km s^{-1} (see also Figure 4b). The velocities are labeled in each panel.

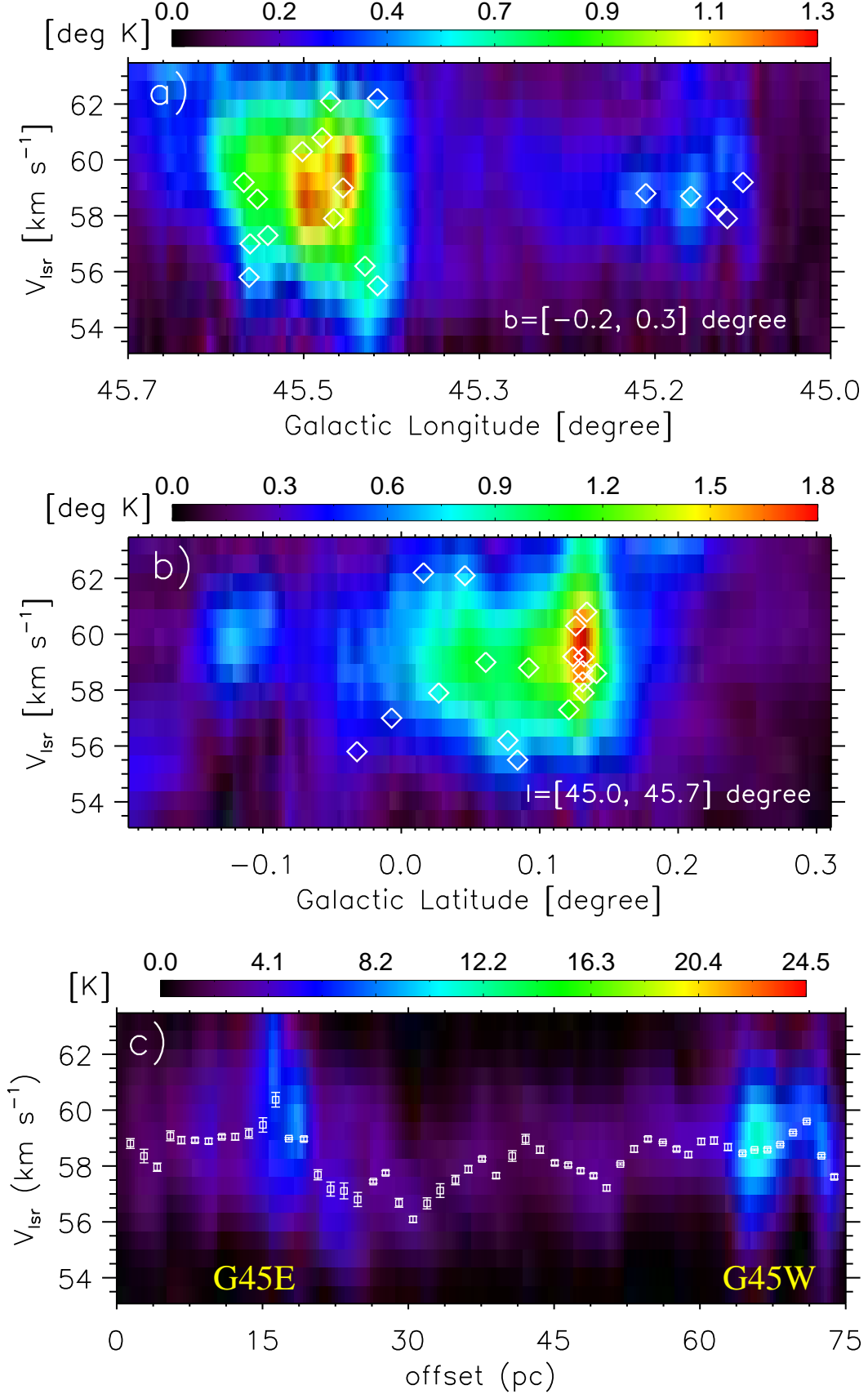


Figure 6. Position-velocity (pv) diagrams of $^{13}\text{CO}(1-0)$ emission: (a) Longitude-velocity diagram, (b) Latitude-velocity diagram, toward an area displayed in Figure 5. The diamond symbols represent the positions of ATLASGAL clumps from [Urquhart et al. \(2018\)](#) (see also Figure 1). (c) The pv diagram along a dashed curve marked in Figure 4a, where zero point in the x-axis corresponds to the eastern end of the curve. The data points with error bars are the velocity averaged points at their respective position (see text for more details).

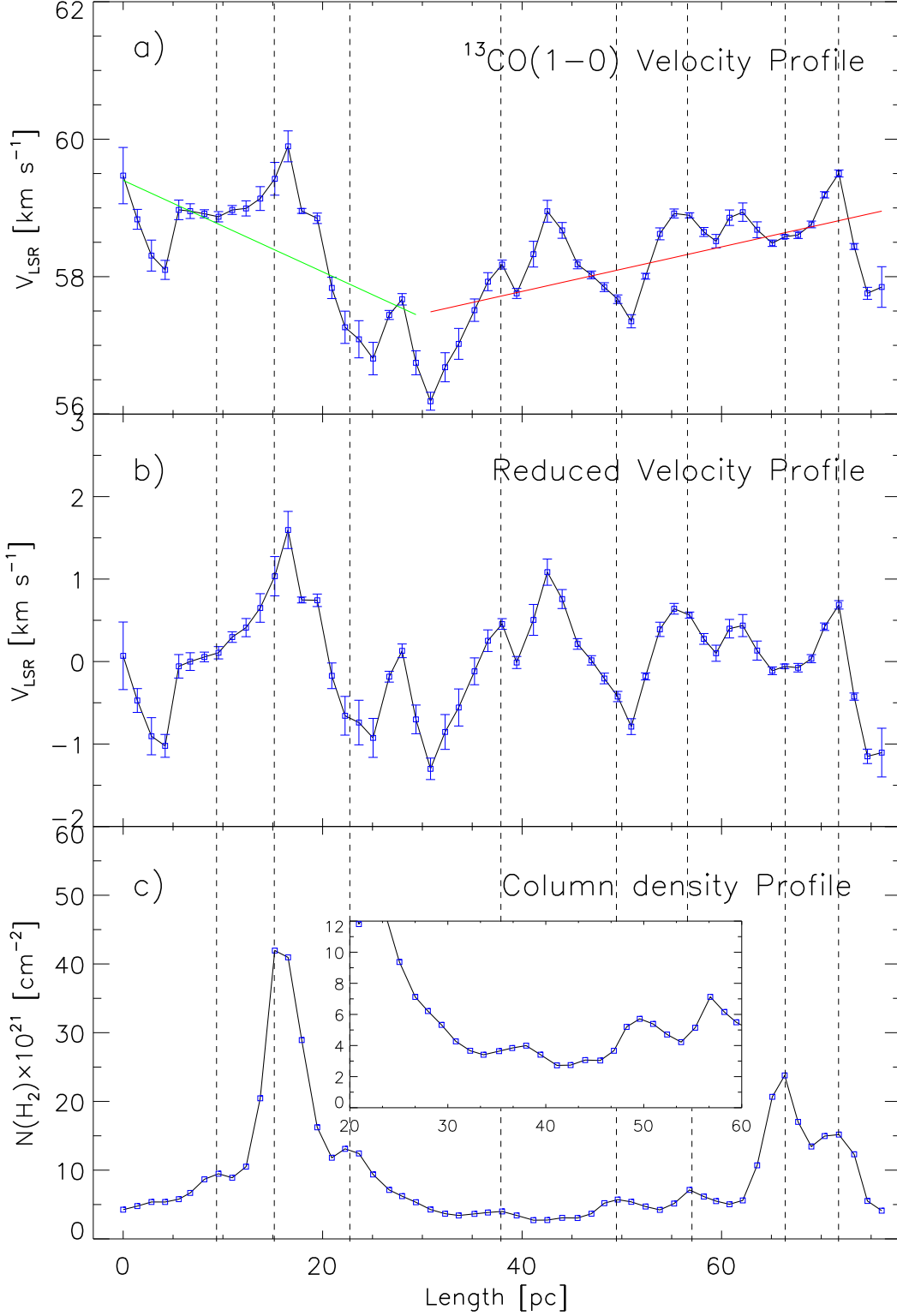


Figure 7. (a) Position-velocity profile of $^{13}\text{CO}(1-0)$ emission, similar to that shown in Figure 6c. The green and red lines indicate the velocity gradient of $-0.064 \text{ km s}^{-1} \text{ pc}^{-1}$ and $+0.032 \text{ km s}^{-1} \text{ pc}^{-1}$, respectively. (b) Residual velocity profile after removing the velocity gradients shown in panel (a). (c) Column density profile. The inset shows a similar column density profile in the length range of 20 to 60 pc.

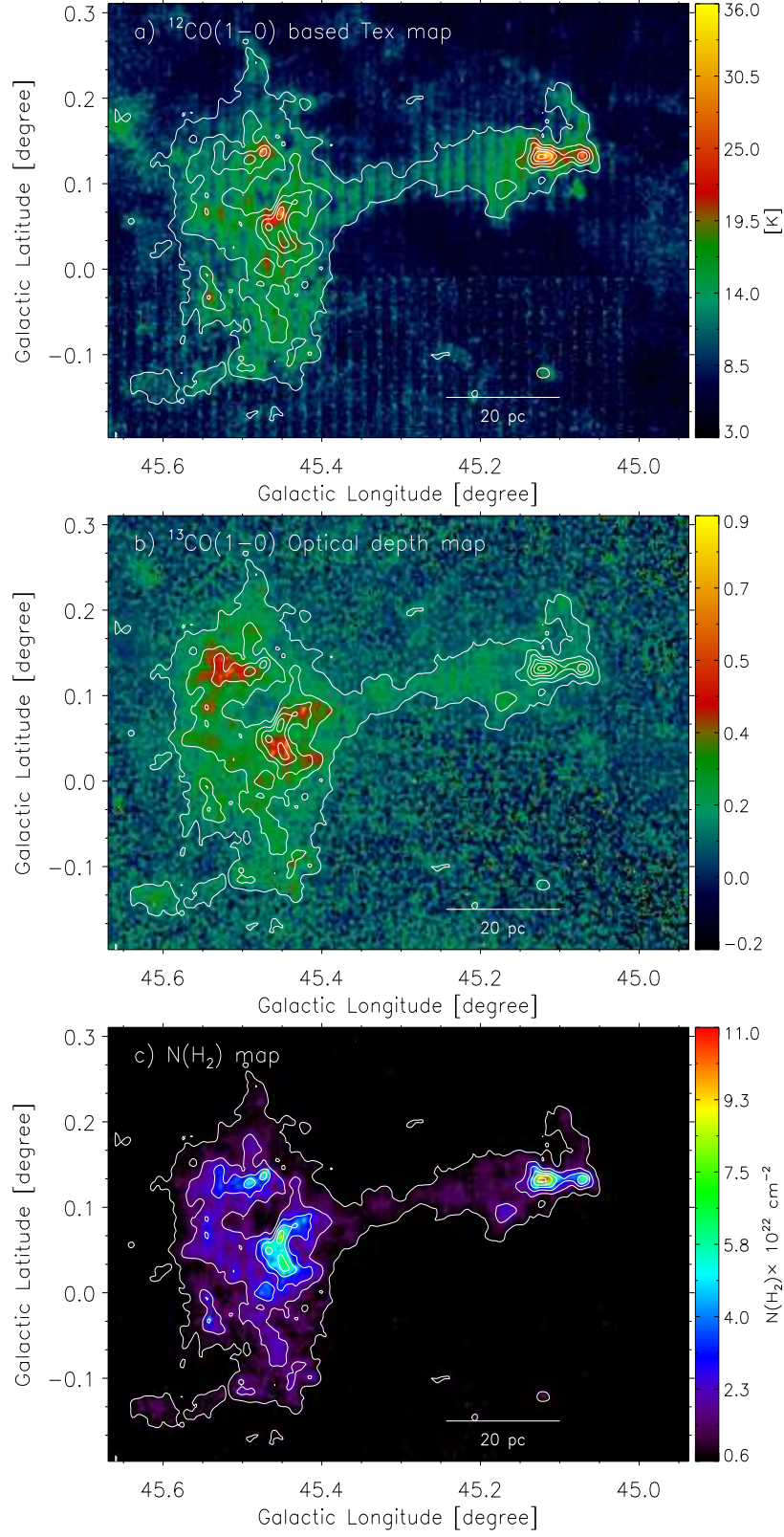


Figure 8. (a) The excitation temperature map derived from $^{12}\text{CO}(1-0)$ emission in the velocity range of $[53, 63] \text{ km s}^{-1}$. (b) $^{13}\text{CO}(1-0)$ optical depth map. (c) H_2 column density map. In all the panels, the contours represent $^{13}\text{CO}(1-0)$ integrated emission ranging from 8 to 60 K km s^{-1} in steps of 10.4 K km s^{-1} .

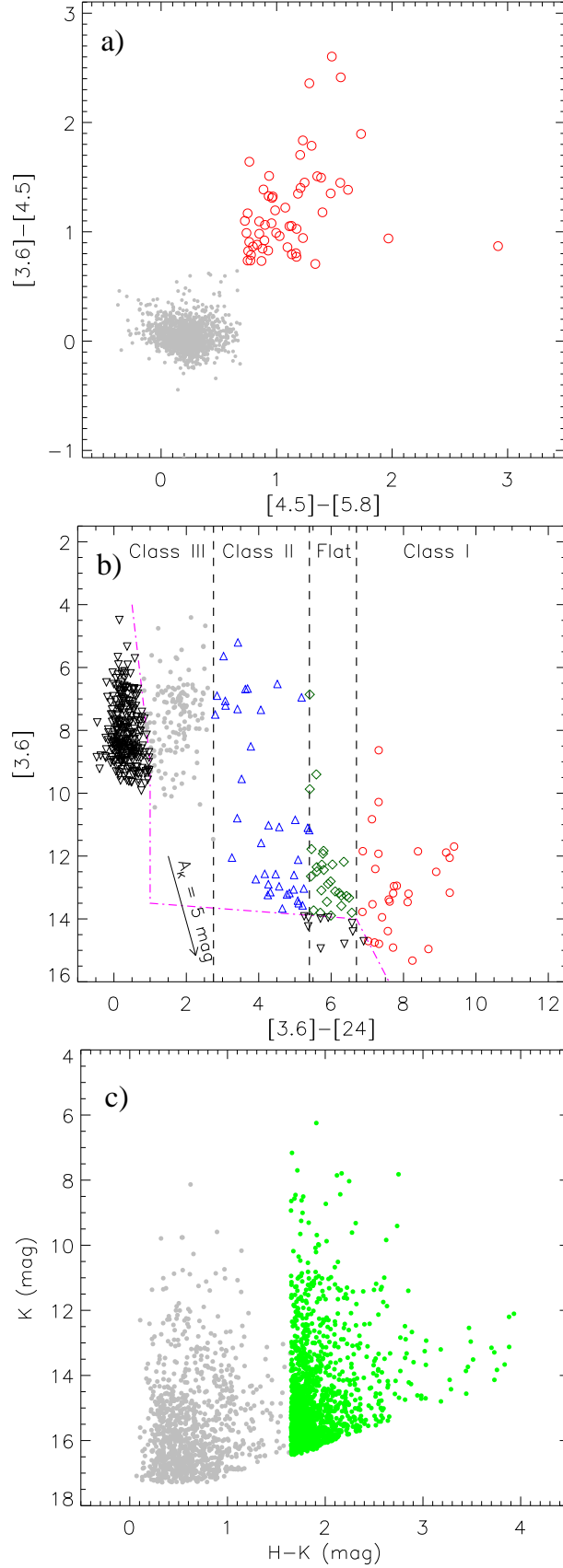


Figure 9. (a) Color-color plot ($[3.6] - [4.5]$ vs. $[4.5] - [5.8]$) of point-like sources in the direction of G045.49+00.04 and G045.14+00.14. (b) Color-magnitude plot ($[3.6] - [24]$ vs. $[3.6]$) of the sources. The plot enables to identify YSOs belonging to different evolutionary stages (see dashed lines). The boundary of YSOs against contaminated candidates (galaxies and disk-less stars) is shown by dotted-dashed lines (in magenta). (c) Color-magnitude ($H - K$ vs. K) diagram of point-like sources. The YSO candidate sources are shown by green dots. In panels “(a)” and “(b)”, the Class I sources are marked by red circles. In all the panels, sources with photospheric emission are shown by dots (in gray), which are randomly drawn from a large sample of our survey catalog.

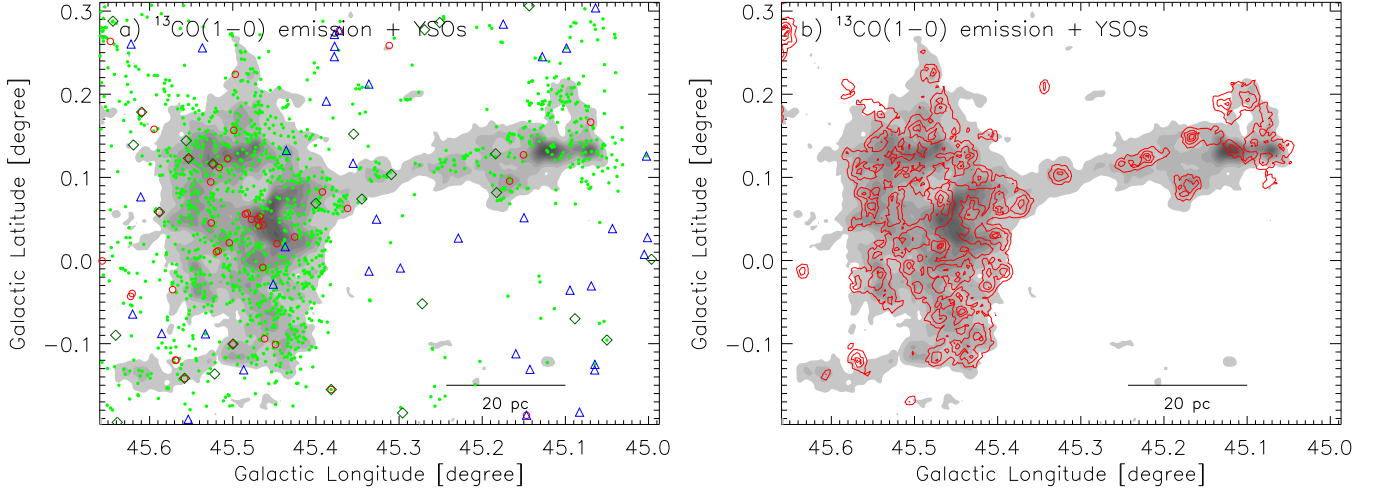


Figure 10. (a) The spatial distribution of YSOs (from Figure 9) overlaid on the $^{13}\text{CO}(1-0)$ integrated intensity map (see Figure 4a). The symbols are same as discussed in Figure 9. (b) Overlay of the YSO surface density contours (in red) on the $^{13}\text{CO}(1-0)$ emission map. The contour values are 0.6, 1.1, 2, 3 YSOs pc^{-2} .

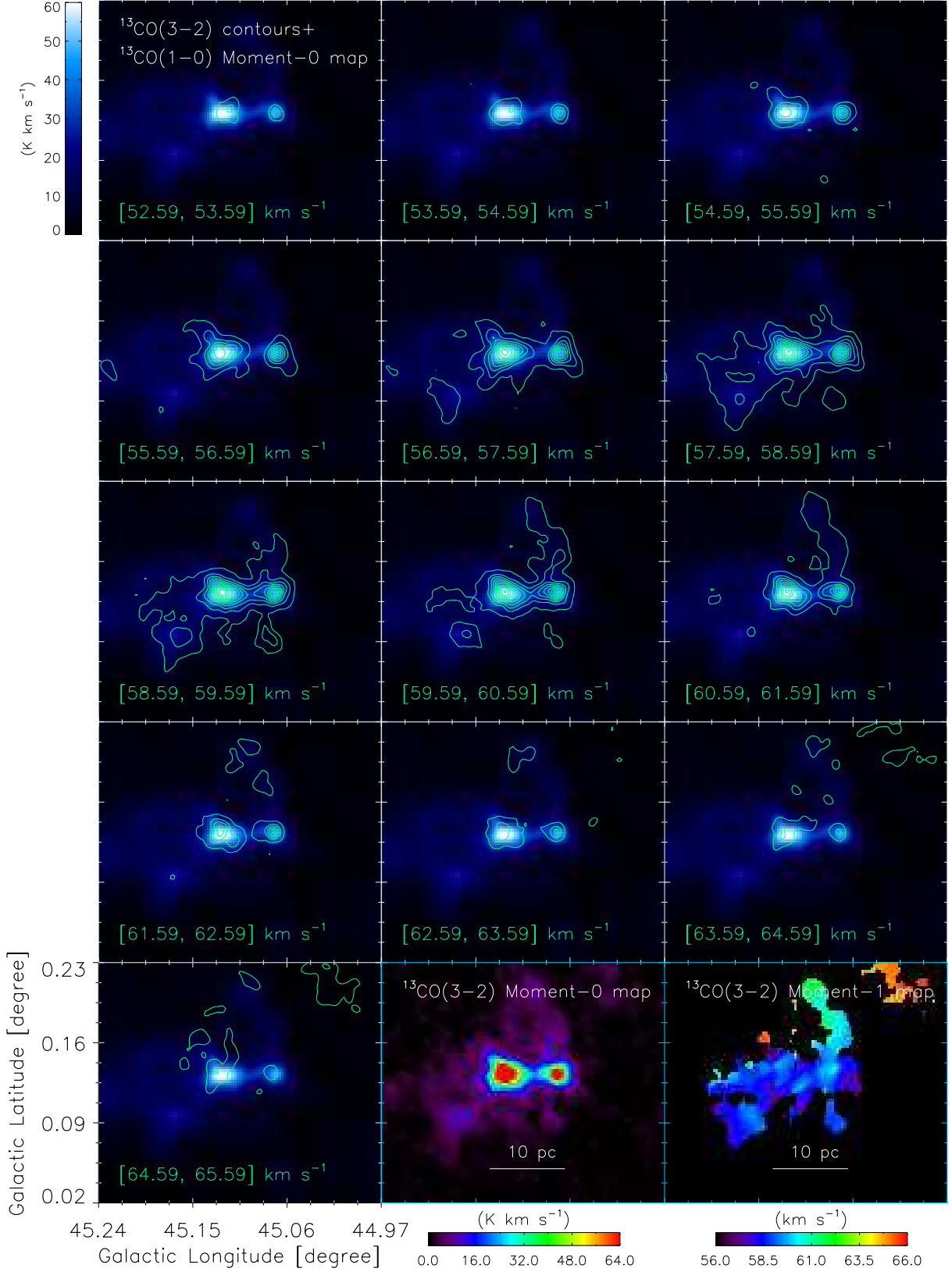


Figure 11. Velocity channel maps of $^{13}\text{CO}(3-2)$ emission (green contours) in the direction of G045.14+00.14 (i.e., G45W) region. The contour levels range from 1.2 to 26 K km s^{-1} in steps of 2.48 K km s^{-1} . The background image is $^{13}\text{CO}(1-0)$ moment-0 map obtained in the velocity range of $[53, 63] \text{ km s}^{-1}$, and the color bar is shown at the top left corner. The last two panels display the moment-0 and moment-1 maps of $^{13}\text{CO}(3-2)$ emission with their respective color bars. The velocities are labeled in each panel.

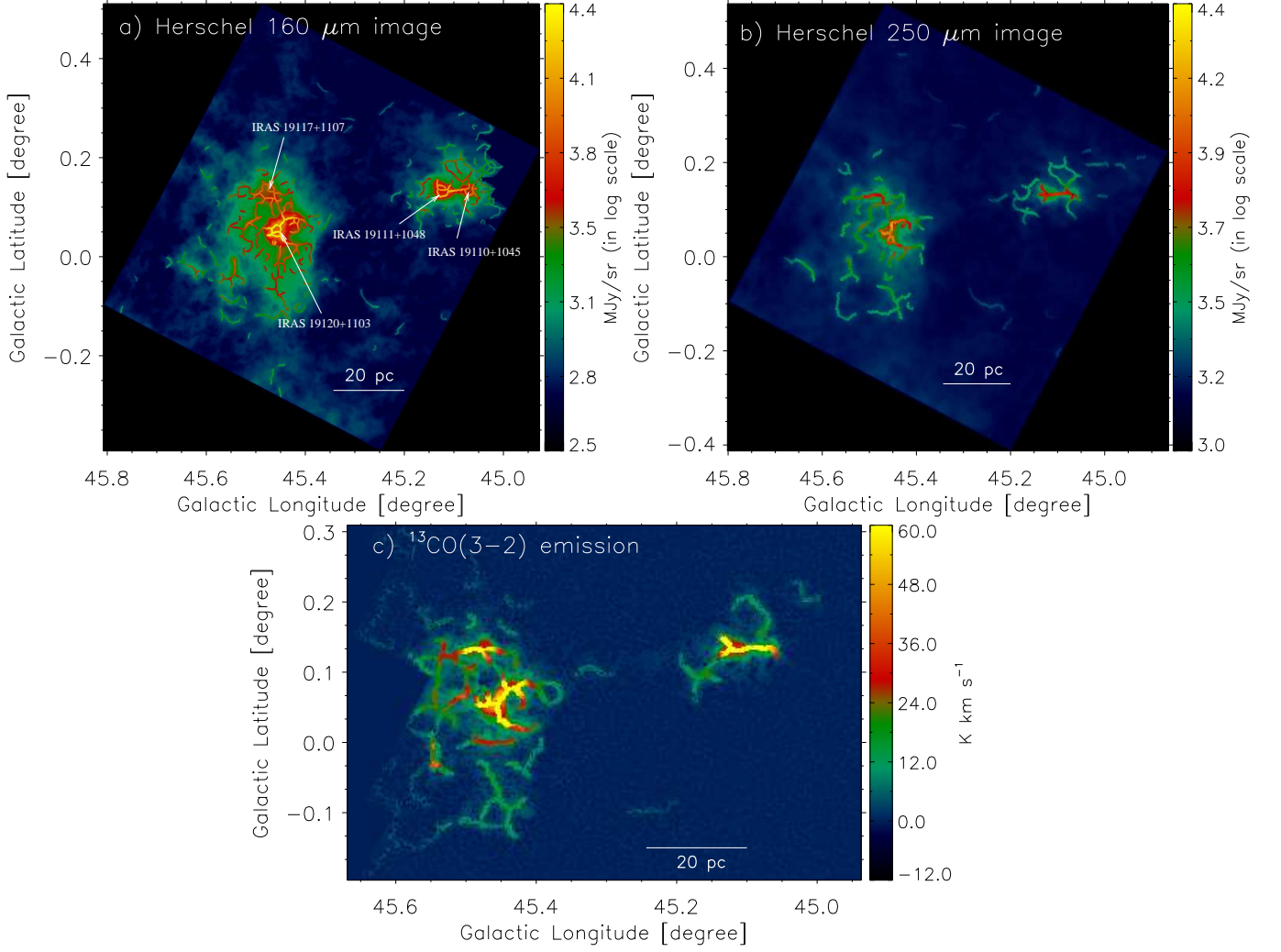


Figure 12. Overlay of the *getsf* identified filament skeletons on the *Herschel* continuum images at (a) 160 μm and (b) 250 μm , and on the (c) CHIMPS $^{13}\text{CO}(3-2)$ moment-0 map (see text for more details). The positions of the IRAS sources are marked by arrows in panel (a).